Available online at www.sciencedirect.com
SCIENCE DIRECT®
Physica D 190 (2004) 213–248
PHYSICA D
www.elsevier.com/locate/physd

Thin liquid films on a slightly inclined heated plate

Uwe Thiele [a,*], Edgar Knobloch [a,b]

[a] *Department of Physics, University of California, Berkeley, CA 94720, USA*
[b] *Department of Applied Mathematics, University of Leeds, Leeds LS2 9JT, UK*

Received 30 May 2002; received in revised form 6 August 2003; accepted 21 September 2003
Communicated by I. Mezic

Abstract

The behavior of a thin liquid film on a uniformly heated substrate is considered. When the substrate is horizontal and the Marangoni number sufficiently large the film breaks up into a periodic array of drops. When the substrate is slightly inclined this drop-like state slides down the substrate. The relation between these states is discussed and their stability properties with respect to longitudinal perturbations are determined. The results shed light on the multiplicity of states accessible to systems of this type and on the possible transitions among them.

PACS: 68.15.+e; 47.20.Ma; 47.20.Lz; 47.20.Ky

Keywords: Heated thin film; Interfacial instability; Marangoni drops; Sliding drops; Kuramoto–Sivashinsky equation

1. Introduction

The study of thin liquid films has a long history [1,2]. Apart from permitting a fundamental simplification of the viscous equations governing free surface flows such films have important technological applications, ranging from the theory of surface coating to the so-called 'printer's' instability [3].

The present paper focuses on the behavior of thin liquid films with a free surface flowing down a slightly inclined smooth solid substrate. The substrate is homogeneously heated and the (infinitely extended) gas layer above it is taken to be passive. Heat transfer from the film surface to the gas is taken into account using Newton's law of cooling at the liquid–gas interface. In the absence of heating the resulting film is stable. However, this is no longer the case once thermocapillary (Marangoni) effects are included, and the resulting instability evolves according to a simplified equation for the film thickness $h(x, t)$ that can be derived from the Stokes equation using a long wave (or lubrication) approximation (cf. [4,5], and references therein). When the substrate is horizontal any instability is necessarily a steady-state instability, since the evolution equation then has a variational structure. However, this is not the case on an inclined substrate, and the instabilities then take the form of a traveling wave. Oron and Rosenau present numerical solutions of the evolution equation in three different cases to identify the structures produced by the instability: these correspond to a film on the upper and lower surface of a horizontal substrate with and without

* Corresponding author. Present address: Max-Planck-Institut für Physik komplexer Systeme, Nöthnitzer Str. 38, D-01187 Dresden, Germany.
E-mail addresses: thiele@mpipks-dresden.mpg.de (U. Thiele), knobloch@physics.berkeley.edu (E. Knobloch).
URL: http://www.uwethiele.de.

0167-2789/$ – see front matter © 2003 Elsevier B.V. All rights reserved.
doi:10.1016/j.physd.2003.09.048

thermocapillarity, and a film flowing down the underside of an inclined substrate without thermocapillary effects [5].

Thermocapillary instabilities are fundamentally longitudinal instabilities that produce structure in the x-direction, although once such structures develop they may in turn be unstable to transverse perturbations. The details depend on the assumptions made concerning the dependence of the surface tension on temperature. This dependence is usually taken to be linear, and the instability that results in two dimensions was studied by Deissler and Oron for a film on the underside of a horizontal substrate [6], with the corresponding results for a film on the upper surface given by Oron [7]. Effects of quadratic capillarity in one dimension were considered by Oron and Rosenau [8] but without including gravity. A similar equation, but for a film below an air layer of finite thickness, was derived by VanHook et al. [9] in connection with their extensive experiments on heated horizontal films, and used to investigate the formation of dry spots. This two-layer formulation leads to a different definition of the Biot number than used below that allows the Biot number to acquire negative values and in consequence richer system behavior. Subsequent work by Boos and Thess followed numerically the evolution of a film profile towards rupture using the full Stokes equation in combination with a linear temperature field [10], and identified a cascade of consecutive "structuring events" pointing towards the formation of a set of drops as the final state of the system. However, due to a slowing down of the numerical scheme once the minimum film thickness becomes very small the final state of the system could not be reached. The qualitative agreement between these results and those obtained from the long wave approximation [7] indicates that the main features of the physical system are well captured by this approximation, as already noted for 'falling' liquid films [2,11]. This terminology refers to liquid films on a strongly inclined substrate. The dynamics of such films differs greatly from the films studied here because inertia enters into the description via the film Reynolds number, and hydrostatic support is insignificant. A number of different evolution equations describing falling films have been proposed [1,12,13], most suffering from the presence of a small parameter, implying that the equation has not been derived by a systematic asymptotic procedure. Nonetheless, within this type of formulation the linear stability properties of a uniform falling film have been studied in detail, and the saturation of the resulting instability determined by weakly nonlinear theory and direct numerical simulation [13–15]. The instability evolves into a nonlinear wavetrain and for heated substrates may lead to film rupture [15]. Transverse instabilities may also be present, leading at long times to a pattern of rivulets with a characteristic transverse wavenumber [16,17]. A recent overview of long wave evolution equations for thin films can be found in Ref. [2].

In the presence of heating horizontal or nearly horizontal films may also be unstable to a short wave convective mode. In contrast to the long wave Marangoni mode this mode is associated with a small surface deformation, and indeed does not require surface deformation at all [18]. The interaction between this mode and the long wave Marangoni mode leads to a number of novel phenomena (e.g. [19] and references therein) but does not occur in the parameter regime considered in the present paper which focuses on dynamics arising from the long wave mode only.

In the present paper we revisit the problem of a heated thin liquid film on a slightly inclined substrate with two motivations in mind: (i) we are interested in the multiplicity of solutions to the nonlinear evolution equation and their stability properties, and (ii) we wish to understand the effects of a small inclination of the substrate. The essence of the problem is captured by a simplified model that omits complications due to effective molecular interactions (disjoining pressure), and the effects of inertia and evaporation. We focus on one-dimensional films, and examine the consequences of a long wavelength longitudinal instability of a flat film that sets in when the Marangoni number exceeds a critical value. On a horizontal substrate we find that the stationary state of the system consists of an array of drops, perhaps separated by dry spots. On an inclined substrate the dry spots are replaced by regions of ultrathin film, and the array of drops slides downslope. We

demonstrate that such sliding trains of drops are a consequence of a Hopf bifurcation from the flat film state, and that they can be stable with respect to longitudinal perturbations. To study these drop arrays we impose periodic boundary conditions in the downstream direction, and formulate the problem as a nonlinear eigenvalue problem for the slide speed and the corresponding thickness profile. Thus all our solutions take the form of a uniformly traveling spatially periodic wave, and correspond to stationary solutions in a suitable moving reference frame. This formulation permits us to study the properties of the resulting solutions as a function of the film parameters and of the spatial period L, and hence to understand the origin of the multiple stable solution branches present at large values of L. Our approach resembles therefore that employed in earlier studies of the Kuramoto–Sivashinsky equation (see [20] and references therein) which appears in some formulations of the falling film problem, but differs from it in employing a more realistic equation for the film, and (more dramatically) in having different symmetry properties. We are able, however, to explore the sequence of transitions that takes place with increasing inclination of the substrate before the Kuramoto–Sivashinsky-like behavior is recovered. For this purpose we employ numerical continuation techniques [21]. These allow us to follow branches of stationary solutions and their bifurcations through parameter space using a Newton-like method [22,23]. In the theory of thin films these techniques have been used with success to study traveling and solitary waves in flow down inclined planes [24], dewetting on a homogeneous substrate [25,26], sliding drops on slightly inclined planes [27,28], transverse instabilities of sliding liquid ridges [29], and rivulet instabilities of thin film flow over a localized heater [30].

The paper is organized as follows. In Section 2 we formulate the basic mathematical problem. In Section 3 we discuss the stationary solutions in the case of a horizontal substrate. These are time-independent and of two types: continuous solutions with thickness bounded away from zero, and discontinuous solutions consisting of drops separated by dry spots. We describe a construction that generates all such solutions and illustrate it with explicit examples. However, we do not address the realizability of these solutions as asymptotic solutions of the initial value problem. In Section 4 we discuss how the solution landscape collapses once the substrate is inclined. The solutions are now devoid of dry spots and all slide down the substrate. These states are obtained by solving a nonlinear eigenvalue problem, and their stability properties can be mapped out by solving an additional linear eigenvalue problem. Some bifurcation-theoretic considerations required for understanding the stability properties of the bifurcation diagrams obtained have been relegated to Appendix A. The paper concludes with a brief discussion. We do not consider transverse instabilities (but see [29]).

2. Film thickness equation

We begin with the evolution equation for the thickness of a thin film flowing down the upper surface of a slightly inclined substrate,

$$h_t = -\left[\frac{h^3}{3}\left(\frac{1}{Bo}h_{xxx} + \alpha - h_x\right) - \frac{h^2}{2}\,Ma\,\partial_x T_s\right]_x . \tag{1}$$

Here $h(x,t)$ is the film thickness in units of its mean thickness h_0, $Ma \equiv \sigma_T \Delta T/\rho g h_0^2$ is the effective Marangoni number of the problem, $Bo \equiv \rho g \ell^2/\sigma_0$ is the Bond number [2], while T_s is the temperature at the surface of the film. The subscripts t, x and the symbol ∂_x denote the corresponding partial derivatives. For a homogeneously heated plate

$$\partial_x T_s = -\frac{Bi\,h_x}{(1+Bi\,h)^2}, \tag{2}$$

where $Bi = \alpha_{th} h_0/k_{th}$ is the Biot number [2]. In deriving Eq. (1) we have nondimensionalized the downslope coordinate x with a characteristic length $\ell \gg h_0$ representing the typical wavelength of the instability, and expressed time in units of the time scale $t_0 = h_0/v_0$, where $v_0 = h_0 u_0/\ell$ and $u_0 = g h_0^3/\nu\ell$ is the characteristic horizontal velocity. In addition we have scaled the pressure with $P_0 \equiv \rho g h_0$ and the temperature with ΔT, the temperature difference across the film. The symbols ρ, ν, σ_0, k_{th}, and α_{th}

denote the density, kinematic viscosity, reference surface tension at temperature T_0, thermal conductivity, and the heat transfer coefficient of the liquid, respectively. The remaining coefficient, σ_T, characterizes the dependence of the surface tension σ on the temperature: $\sigma = \sigma_0 - \sigma_T(T - T_0)$. These equations are derived in Ref. [5] (their Eq. (43) with $N = 1$); the temperature gradient at the surface, Eq. (2), results from the assumptions of constant temperature at the plate and Newton's law of cooling at the free surface of the film [2]. In the horizontal limit ($\alpha = 0$) Eq. (1) corresponds to Eq. (2.63) of Ref. [2]; with $\alpha = O(1)$ it can also be derived as the small inclination limit of the falling film equation, Eq. (3.13) in Ref. [15], on dropping the effects of evaporation. Note that, as defined here, the Marangoni number *Ma* corresponds to M/G in [2] and to M/GP in [15]; in some papers (e.g. [10]) *Ma* is referred to as the inverse dynamic Bond number, while *Bo* is called the static Bond number.

Eq. (1) is valid under two assumptions [5]: (a) small inclination angles required for the retention of the hydrostatic pressure term, and (b) small values of the Reynolds number $Re = u_0 h_0/\nu$ to justify the dropping of inertial terms (the Reynolds number in [9] is 10^{-4}). In the scaling used here the plane makes an angle $\alpha h_0/\ell$ to the horizontal, a quantity that is small provided ℓ is taken to be sufficiently large. The four terms on the right-hand side of Eq. (1) then describe the effects of capillarity, and driving by gravity, hydrostatic pressure and the Marangoni force, respectively. For a film on the underside of an inclined plate the sign of the hydrostatic term is reversed.

Since the vertical length scale used is the mean film thickness, h_0, the flat (uniform) film corresponds to the solution $h(x) = 1$. This solution is unstable with respect to infinitesimal perturbations of the form $\exp(\beta t + \mathrm{i}kx)$ for Marangoni numbers above a critical value, Ma_c, given by

$$Ma_c = \frac{2}{3}\frac{(1+Bi)^2}{Bi}. \tag{3}$$

The wavenumber at onset is zero. Above Ma_c the flat film is unstable to perturbations with wavenumbers $0 \le k \le k_c$, where k_c is given by

$$k_c^2 = Bo\left(\frac{Ma}{Ma_c} - 1\right). \tag{4}$$

In the following we study Eq. (1) on a periodic domain $0 \le x < L$; by varying L we can admit different numbers of the most unstable wavelengths $2\sqrt{2}\pi/k_c$. Due to translation invariance the resulting problem has the symmetry O(2) (if $\alpha = 0$) or SO(2) (if $\alpha \neq 0$). This change in symmetry when α becomes nonzero turns the primary bifurcations from the flat state from pitchforks of revolution into Hopf bifurcations that create traveling waves [31]. The resulting traveling waves may still be viewed as steady states, but only in an appropriately moving reference frame. When formulated this way the speed v of the frame becomes a nonlinear eigenvalue; this speed depends on the amplitude of the wave (more precisely on its degree of left–right asymmetry) and hence on the distance above the critical Marangoni number. All these solutions satisfy the constraint

$$\bar{h} \equiv \frac{1}{L}\int_0^L h(x,t)\,\mathrm{d}x = 1, \tag{5}$$

i.e., that the mean thickness of the film is constant. Since $\int_0^L h(x,t)\,\mathrm{d}x$ represents the 'volume' V of the film in one spatial period, we conclude that the volume remains constant during evolution, with $V = L$ at all times. Note that we can always choose $\ell = L$ and hence write Eq. (1) on the domain $0 \le x < 1$. We prefer, however, to think of ℓ as chosen once and for all so that both *Bo* and the angle α have fixed values, and then examine the effects of increasing the spatial period L, thereby admitting longer and longer scales into the problem, and permitting the development of coarsening instabilities. Alternatively we can choose the length scale ℓ such that $Bo = 1$, i.e., $\ell = \sqrt{\sigma_0/\rho g}$.

Eq. (1) can be written in the general form

$$h_t = -\left[Q(h)\left(\alpha + \left(\frac{h_{xx}}{Bo} - f_h(h)\right)_x\right)\right]_x, \tag{6}$$

where $Q(h) = h^3/3$ is the mobility factor and $f(h)$ is a free energy, that in the present case takes the form

$$f(h) = \frac{1}{2}h^2 - \frac{3}{2}\,Bi\,Ma\,h\,\log\left(\frac{h}{1+Bi\,h}\right). \tag{7}$$

Thus $f(0) = 0$ and, when $Bi > 0$, $Ma > 0$, $f(h)$ increases with h, although not necessarily monotonically. When $\alpha = 0$ Eq. (6) takes the form of a Cahn–Hilliard equation familiar from spinodal decomposition of a binary mixture [32–34] and dewetting of a thin liquid film [35–39] albeit with a different potential f, while for $\alpha > 0$ it resembles the driven Cahn–Hilliard equation [40] or the equation describing sliding drops or fronts on an inclined plane [27,41,42]. Eq. (6) with $\alpha = Ma = 0$ and the opposite sign for $f(h)$ describes the instability of a thin liquid film bounded by a substrate and a heavier overlying liquid [43]. Consequently, some of the general results for these systems, particularly those for stationary solutions [26,39,43], apply here as well.

3. The horizontal substrate

On a horizontal substrate ($\alpha = 0$) the film equation takes the form

$$h_t = -[Q(h)(h_{xx} - f_h(h))_x]_x, \tag{8}$$

where we have set $Bo = 1$ since the solutions $h(x)$ for $Bo \neq 1$ can be recovered from those for $Bo = 1$ by stretching the x-coordinate by $\sqrt{1/Bo}$. The results that follow are computed for the case $Bi = 0.5$. This equation has variational structure with the quantity

$$E[h] \equiv \frac{1}{L}\int_0^L \left[\frac{1}{2}h_x^2 + f(h) - f(1)\right] \mathrm{d}x \tag{9}$$

as the corresponding Lyapunov functional [5,39]. This structure has an important consequence: no oscillations are possible and hence no primary or secondary bifurcations to traveling or standing waves can take place. The system therefore evolves monotonically towards the minima of E. These correspond to stationary solutions $h(x)$ which satisfy

$$h_x = \sqrt{2[f(h) - C_1 h - C_2]}. \tag{10}$$

Here C_1 and C_2 are two constants of integration. We define the quantities h_i and h_m such that

$$C_1 = f_h(h_\mathrm{i}), \qquad C_2 = f(h_\mathrm{m}) - C_1 h_\mathrm{m}. \tag{11}$$

Thus the thickness $h = h_\mathrm{i}$ corresponds to the location of an inflection point in the film profile ($h_{xx} = 0$), while $h = h_\mathrm{m}$ corresponds to either maximum or minimum thickness ($h_x = 0$), depending on the sign of h_{xx}. For localized solutions we take $h_\mathrm{m} = h_\mathrm{i} = h_\infty$, where h_∞ denotes the film thickness in the far field. It is convenient therefore to think of the steady solutions as being parametrized by the quantities h_i, h_m instead of C_1 and C_2. The different possible solutions $h(x)$ may be computed explicitly by numerical integration and represented in the phase plane (h, h_x) for different values of h_i, h_m. They can also be discussed in terms of a 'potential' $g(h)$ defined by $g(h) \equiv f(h) - C_1 h$. Physically $g(h)$ is the energy per unit length of a depression of finite length and thickness h in an infinitely extended thin film with asymptotic thickness $h_\infty = 1$. The energy $g(h)$ is plotted for different values of Ma in Fig. 1. Observe that $g(h)$ may have one (if $Ma = 0$) or two (if $Ma > 0$) minima. The flat film at $x \to \pm\infty$ ($h_\infty = 1$) corresponds to a global energy minimum for $0 < Ma < 1.0$, remains a local minimum (i.e., metastable) for $1.0 < Ma < 3.0$, and is linearly unstable for $Ma > 3.0$. The local minimum that develops at $h = 0$ for $Ma > 0$ indicates the existence of solutions in the form of liquid drops separated by "dry spots" where the film thickness vanishes.

As already mentioned, the periodic solutions can also be parametrized using the mean film thickness $\bar{h}$ and their 'volume' V (or spatial period L) instead of the quantities h_i, h_m. Since $\bar{h} = 1$ due to the scaling

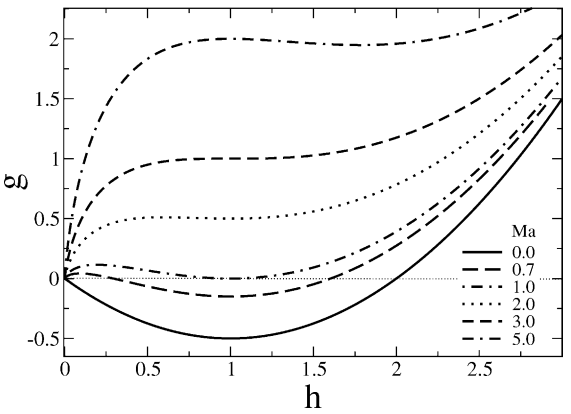

Fig. 1. The energy $g(h) \equiv f(h) - C_1 h$ for different values of Ma and $Bi = 0.5$ showing global and local minima. The film is linearly unstable for $Ma > 3$ for which $h = 1$ is a maximum.

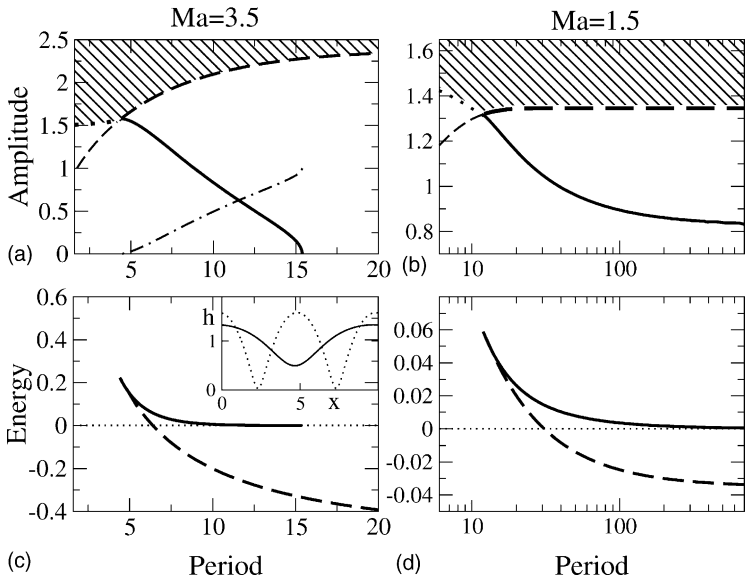

Fig. 2. The periodic nucleation and single drop solutions for $Bi = 0.5$ and $Bo = 1.0$ in (a) the linearly unstable ($Ma = 3.5 > Ma_c$) and (b) the metastable ($Ma = 1.5 < Ma_c$) regime as a function of L. The solid and dashed-dotted lines show $h_{max} - h_{min}$ and h_{min} for the nucleation solutions; h_{min} vanishes at the cusp on the left, located at $(L^\star, h^\star)$. The thick (thin) dashed line shows allowed (forbidden) single drop solutions with $\theta_0 = 0$, and asymptotes to $h = h_{crit}$ as $L \to \infty$. Stable single drop solutions with $\theta_0 > 0$ are found in the hatched region above this line. Panels (c) and (d) show the corresponding relative energies per unit length $E(L)$. The inset in (c) shows the film thickness profiles for the nucleation solutions at $L = 5$ (dotted) and $L = 10$ (solid). Profiles for the drop solutions can be found in Fig. 5.

used there remains a one parameter family of solutions for each combination (*Ma*, *Bi*). Fig. 2 shows this family in terms of the amplitude $\Delta h \equiv h_{max} - h_{min}$ and the relative energy per unit length E (Eq. (9)) as functions of the spatial period L (thick solid lines). Fig. 2(a) shows the results when the flat film is unstable: a one parameter family of steady solutions bifurcates subcritically from the flat film for which $\Delta h = 0$. These solutions are all unstable, and we refer to them as *nucleation* solutions. This is because an initial perturbation with amplitude less than Δh (and $\bar{h} = 1$) will decay to the flat film, while one with larger amplitude will evolve to a drop-like state, as discussed further below. This family of nucleation solutions terminates at a finite value of L, $L = L^\star$, where the minimum thickness h_{min} (dashed-dotted line) drops to zero and $h_{max} = h^\star$, satisfying $f(h^\star) - f_h(h_i)h^\star = 0$. Nucleation solutions are present even when the flat film is stable (see Fig. 2(b)), but the corresponding solution branch is now disconnected. We say in this case that the flat film state is *metastable*.

When the flat film is unstable the branch of nucleation solutions shown in Fig. 2(a) is only the first of an infinite number of primary solution branches. These bifurcate from the flat film state at $L = L_n \equiv 2\pi n/k_c$, $n = 1, 2, \ldots$, where k_c is given by Eq. (4). In the following we use the integer n to label the resulting primary branches. Each of these branches terminates in a singular point, with $L_n^\star = nL^\star$ and identical critical amplitude $h_{max} = h^\star$ (see Fig. 4). These limiting solutions consist of the $n = 1$ limiting solution replicated n times in a domain of period $nL^\star$, i.e., they consist of n identical drops each just touching its neighbors.

Fig. 2(a) and (c) reveal that solutions exist even for $h_{max} > h^\star$. These solutions occupy the hatched region in the figures and correspond to *two* parameter families of 'dry spot' or 'hole' solutions. For these solutions the fixed mean film thickness no longer reduces the dimension of the solution space: the individual drops can be spaced arbitrarily and every solution can be distributed periodically in such a way that it fulfills the requirement $\bar{h} = 1$. There are three conditions that

restrict the allowed range of (h_i, h_{max}) for this class of solutions:

(i) The individual drops are not allowed to overlap. In practice, this condition is only important for periods smaller than the minimal period $L^\star$ on the nucleation branch. This condition determines the dotted boundary of the hatched region in Fig. 2(a) and (b).

(ii) For this type of solution the microscopic contact angle $\theta_0 \equiv h_x|_{h=0}$ has to exist, i.e., the expression under the square root on the right-hand side of Eq. (10) must be non-negative even at $h = 0$. Thus $f_h(h_i)h_{max} - f(h_{max}) \geq 0$. The dashed lines in Fig. 2(a) and (b) represent the limiting solutions with $\theta_0 = 0$. These bound the hatched region for $L > L^\star$ (thick dashed lines), but have no physical meaning for $L < L^\star$ (thin dashed lines) since they enter a region where the period of the solution would be smaller than the corresponding drop width (see Fig. 3).

(iii) The slope h_x at the maximum of the profile h_{max} has to be a real zero, i.e., $f_h(h_i) - f_h(h_{max}) \geq 0$. Unlike cases (i) and (ii) this condition does not result in a line in the (L, h_{max}) plane but limits the allowed range of h_i for a given h_{max}. This limit is more restrictive than the limit arising from (ii) only for $h_{max} > h_{crit}$, where h_{crit} satisfies

$$f_h(h_{crit})h_{crit} - f(h_{crit}) = 0, \tag{12}$$

i.e.,

$$h_{crit} = -\frac{1}{2Bi} + \sqrt{\frac{1}{4Bi^2} + 3Ma}, \tag{13}$$

obtained by setting the conditions resulting from (ii) and (iii) both equal to zero. The thick dashed lines in Fig. 2(a) and (b) representing a one parameter family of 'hole' solutions with $\theta_0 = 0$ (Fig. 3) thus originate at $L^\star$ and diverge to infinite L at h_{crit}; no solutions with $h_{max} > h_{crit}$, $\bar{h} = 1$ and zero microscopic contact angle are possible. Once again the limiting drop solutions can be replicated n times to obtain periodic multidrop solutions with period nL. Each of the resulting solution branches originates at $L = nL^\star$, $h_{max} = h^\star$ and diverges to infinite L as h_{max} approaches h_{crit}. These branches, labeled by the corresponding integer n, are also shown in Fig. 4.

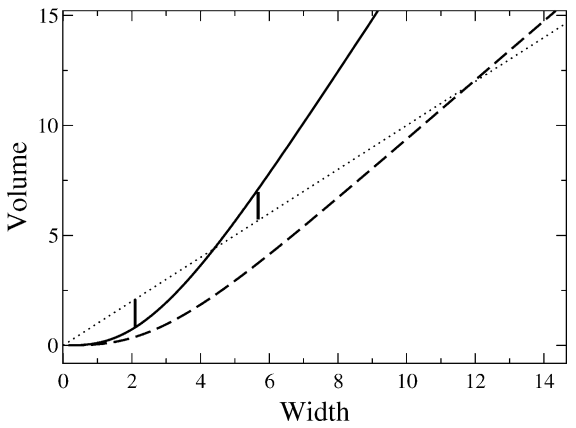

Fig. 3. The drop volume L as a function of its width w for $Ma = 3.5$ (solid line) and $Ma = 1.5$ (dashed line) along the thick dashed line in Fig. 2. The dotted line indicates the relation $L = w$. The intersections define the points $L^\star$. Dry spots are present when $L > w$. The vertical lines indicate the construction of a two-drop solution corresponding to the maximum along the 1:1 branch in Fig. 4 (see text).

Fig. 2(c) and (d) show the energy E for the nucleation solutions (thick solid lines) and the hole solutions with $\theta_0 = 0$ (thick dashed lines). The hole solutions with $\theta_0 \neq 0$ (not shown) always have *higher* energy than the corresponding $\theta_0 = 0$ solutions. Thus the $\theta_0 = 0$ solutions are energetically favored, a fact that we use as a selection mechanism in the absence of a disjoining pressure in Eq. (1) to describe partial wetting. The disjoining pressure originates in the interaction between the fluid molecules and those of the substrate and acts on length scales below 100 nm [2], i.e., much smaller than the mean thickness of the film. Such a pressure also selects a unique solution branch from within the hatched region in Fig. 2 but this solution differs from the one selected on the basis of the above energy argument since the selected microscopic contact angle will be *nonzero*.

Fig. 5(a) and (b) show two series of possible drop profiles, each obtained for identical values of the parameters (*Ma*, *Bi*, *Bo*) *and* fixed volume $V = L$. Fig. 5(a) is computed for $Ma = 3.5$, $Bi = 0.5$, $Bo = 1.0$, corresponding to a linearly unstable uniform film,

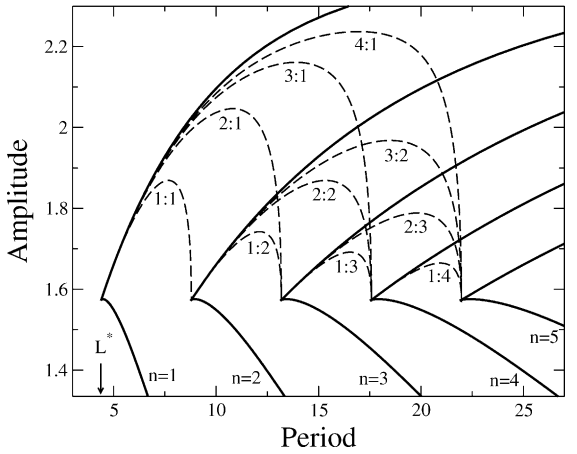

Fig. 4. The amplitude $\Delta h \equiv h_{\max} - h_{\min}$ along single drop and multidrop branches with microscopic contact angle $\theta_0 = 0$ as a function of L when $Ma = 3.5$, $Bi = 0.5$ and $Bo = 1.0$ (cf. Fig. 2(a)). The solid lines show the primary $n = 1, \ldots, 5$ branches consisting of periodic nucleation solutions (lower part) and the periodic single drop solutions (upper part) obtained by replication of the $n = 1$ solution. The dashed lines show the different possible multidrop branches with maximal internal symmetry and no dry holes. Multidrop solutions with broken internal symmetry are present between these multidrop branches as described in the text. Every multidrop solution of this type in turn represents the starting point for $i + j$ branches containing finite dry holes.

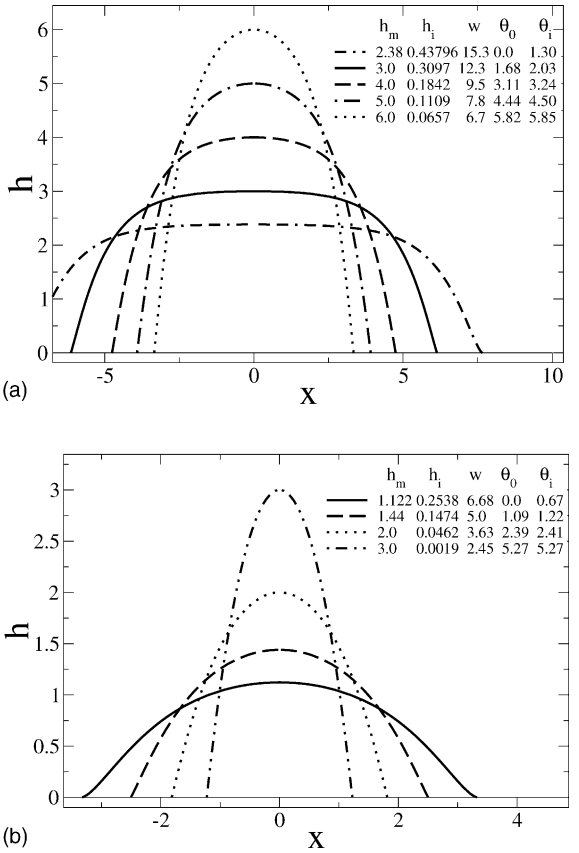

Fig. 5. Different drop profiles for $Bi = 0.5$, $Bo = 1.0$ and fixed volume (a) $L = 30$, $Ma = 3.5$, (b) $L = 5$, $Ma = 1.5$. The maximum thickness $h_{\max}$, the thickness h_i at $h_{xx} = 0$ and the width w of the drop are listed, as are the contact angles $\theta_0 = h_x(0)$ and $\theta_i = h_x(h_i)$.

and the drops shown all have volume $V = 30.0$. In contrast Fig. 5(b) is for $Ma = 1.5$, $Bi = 0.5$, $Bo = 1.0$, corresponding to a metastable flat film, and $V = 5.0$. The insets in the figure give the width w of the drops and the contact angles determined from Eq. (10): the microscopic contact angle at $h = 0$ given by $\theta_0 = h_x|_{h=0}$ and the mesoscopic contact angle defined as the slope at h_i: $\theta_i = h_x|_{h=h_i}$. These angles are shown as a function of $h_{\max}$ for several different values of L in Fig. 6. The solid profile in Fig. 5(a) corresponds to a solution on the thick dashed line in Fig. 2(a). However, the corresponding solution in Fig. 5(b) is "forbidden" because its width $w > 5$, in conflict with the requirement (i) above. The next drop shown (dashed line) is the limiting drop with $w = L$. This solution has $\theta_0 > 0$ and so lies *above* the thick dashed line in Fig. 2(b). Fig. 3 shows graphically the extent of the dry spots for these two values of Ma, $Ma = 3.5$ (solid line) and $Ma = 1.5$ (dashed line). The figure shows the volume V (i.e., the spatial period L) as a function of the width w of the drop. Allowed single drop solutions exist above the dotted curve $V = w$ since for such drops $w < L$. The extent of the dry spot, i.e., $L - w$, is then given by the distance between the curve $V(w)$ and the line $V = w$. The intersection of these two curves marks the location of $V(w) = w = L^\star$. Note that the dry spots are larger for larger Ma. This is because the increased temperature dependence of the surface tension holds the drop together more effectively. Fig. 7 shows the contours of the flow inside each drop obtained from the lubrication approximation,

$$\mathbf{u} = (\psi_z, -\psi_x) \tag{14}$$

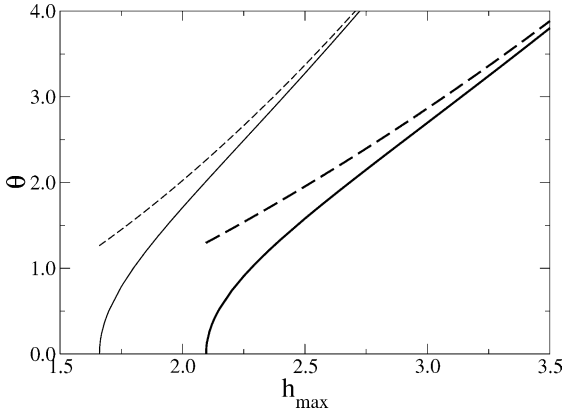

Fig. 6. The microscopic (θ_0, solid lines) and mesoscopic (θ_i, dashed lines) contact angles as a function of the maximum film thickness when $Bi = 0.5$, $Bo = 1.0$, $Ma = 3.5$ and fixed volume $L = 5$ (thin lines) and $L = 10$ (thick lines).

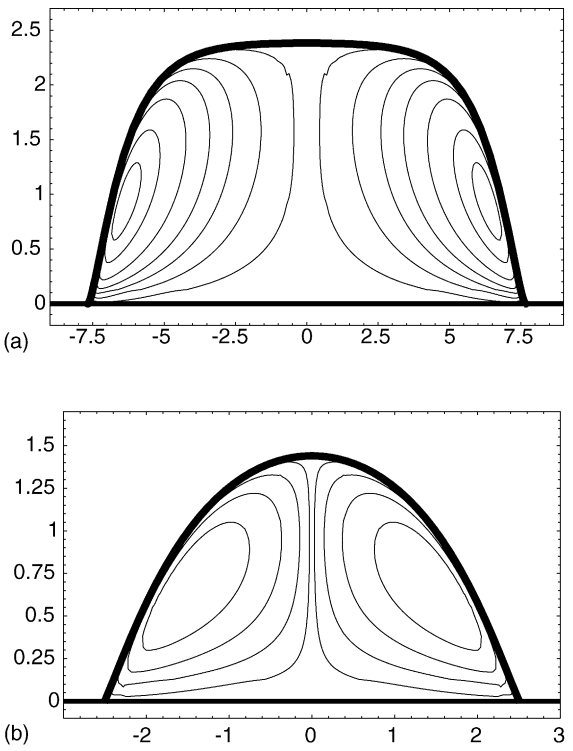

Fig. 7. The streamlines inside a drop with (a) $\theta_0 = 0$ when $Bi = 0.5$, $Bo = 1.0$, $Ma = 3.5$, $L = 30$, $\psi = \pm 0.000205, \pm 0.001, \pm 0.0025, \pm 0.005, \pm 0.01, \pm 0.02, \pm 0.03$; and (b) $w = L$ when $Bi = 0.5$, $Bo = 1.0$, $Ma = 1.5$, $L = 5$, $\psi = \pm 0.0002, \pm 0.001, \pm 0.0025, \pm 0.005, \pm 0.01, \pm 0.02, \pm 0.03$. The flow descends from the apex where cooling is strongest.

with the streamfunction ψ given by

$$\psi(x,z) = \left(\frac{z^2 h}{2} - \frac{z^3}{6}\right)\left(\frac{1}{Bo}h_{xxx} + \alpha - h_x\right) + \frac{z^2}{2}\frac{Ma\,Bi\,h_x}{(1+Bi\,h)^2}. \tag{15}$$

This flow is a consequence of the thermal gradient along the free surface of the drop due to heat loss from its surface, and takes the form of an outward flow along the (heated) bottom of the drop and its replenishment by cooler liquid descending from its apex. The vigor of this circulation determines the contact angles θ_0 and θ_i. Such flows are of course absent from liquid drops that form on an unheated horizontal substrate as a result of a molecular interaction between the substrate and the fluid, i.e., via the inclusion of a disjoining pressure in the hydrodynamic formalism [38,39], even though the governing equation has the same structure as our Eq. (8) and the shapes of the resulting drops are quite similar.

Thus far we have only discussed periodic arrays of drops, containing only a single drop per spatial period. These periodic solutions are linearly stable, and no coarsening can occur because no liquid can pass across the dry zones where $h = 0$. This is due to the absence from the model of additional interactions between the substrate and the film. A consequence of this fact is that drops of different sizes can be distributed arbitrarily provided they do not overlap and their overall volume matches the total occupied space. Because of the dry substrate between the drops the resulting configurations are all linearly stable. However, the dependence of the energy E on the period L implies that only the single drop solution whose period matches the system size is absolutely stable, as in the corresponding dewetting problem [39].

Arbitrarily spaced drops on a homogeneous surface should have identical microscopic contact angle. Within our model we must demand that this angle be zero, i.e., we take drops on the dashed line in Fig. 2(a) or (b), respectively. Individual drops in a multidrop solution of period L are no longer restricted by the requirement (i) which only applies to the overall solution. Thus a general n-drop solution without finite

dry holes must satisfy

$$\sum_{i=1}^{n} V(w_i) - w_i = 0. \tag{16}$$

Every n-drop solution fulfilling this condition provides a starting point for an infinite number of solution branches with dry holes of finite length between the individual drops obtained by replacing one or more drops of width w_i by drops of width $\tilde{w}_i$ with $V(\tilde{w}_i) > V(w_i)$, provided only that $\mathrm{d}V(w)/\mathrm{d}w|_{w_i} > 1$ for these drops (cf. Fig. 3). This is a consequence of the fact that the total volume determines the spatial period L via Eq. (5). The resulting dry interval $\sum V(\tilde{w}_i) - \tilde{w}_i$ can be distributed arbitrarily among the n interdrop intervals. Note that drops with $w_i < L^\star$ do not constitute solutions in their own right but must be combined with others with $w_j > L^\star$ to produce an admissible solution.

We now discuss, somewhat in the spirit of Ref. [43], the possible solutions in the simplest case of two drops per period, and sketch the results for the case with three or more drops.

Two drops: If the width of each of the constituent drops exceeds $L^\star$ all drop combinations are allowed. Since $V(w_1) + V(w_2)$ is the total volume of the two drops, the spatial period L of the solution follows from the requirement $[V(w_1) + V(w_2)]/L = \bar{h} = 1$, i.e., $L = V(w_1) + V(w_2)$. The dry length in one period is therefore $V(w_1) - w_1 + V(w_2) - w_2 > 0$, and this can be distributed arbitrarily since the drops do not interact.

If, however, the width of one of the drops is smaller than $L^\star$, i.e., a solution forbidden as a single drop solution, the second drop must fulfill the condition $V(w_2) - w_2 > -(V(w_1) - w_1)$. Fig. 3 shows that for every drop with $w_1 \leq L^\star$ there is exactly one second drop with $V(w_2) - w_2 = -(V(w_1) - w_1)$ (Eq. (16) with $n = 2$). Such a solution does not admit dry spots and therefore has period $L = w_1 + w_2$. To compute this branch we turn the above relations into a plot of the amplitude as a function of L. The resulting curve starts at the singular point on the primary $n = 1$ branch where $w_1 = 0$, $w_2 = L^\star$ and terminates at the singular point on the primary $n = 2$ branch where $w_1 = w_2 = L^\star$, and is indicated in Fig. 4 by the dashed line labeled 1:1. The thick vertical lines in Fig. 3 correspond to the *maximum* amplitude along the 1:1 branch. Branches of solutions with dry spots fill the region in Fig. 4 above the 1:1 branch.

Three drops: Solutions consisting of three drops with no dry holes between them can be constructed in the same way. In general once the first drop is fixed the remaining volume can be distributed among the remaining two drops at will. If, however, we impose additional internal symmetries a unique solution branch is selected.

(i) For example, we may assume that two identical drops with $w < L^\star$ are combined with one drop with $w > L^\star$. For every such pair there is exactly one possible third drop with $V(w_3) - w_3 = -2(V(w_1) - w_1)$. Calculating w_3 for all $0 \leq w_1 \leq L^\star$ yields the branch denoted by 2:1 in Fig. 4 connecting the singular points at $L^\star$ and $3L^\star$ on the $n = 1$ and $n = 3$ primary branches, respectively.

(ii) If, on the other hand, we combine two identical drops with $w > L^\star$ with one drop with $w < L^\star$ we obtain the branch labeled in Fig. 4 by 1:2. This branch connects the singular points with periods $2L^\star$ and $3L^\star$ on the $n = 2$ and $n = 3$ primary branches, respectively.

It is possible to check that by breaking the internal symmetries imposed above one can obtain any state between the curves 1:1, 1:2 and 2:1 in Fig. 4.

Multiple drops: We can insert any number i of drops of zero width at the singular point $L = L^\star$ on the $n = 1$ branch, and each of these can be followed in L, giving rise to the family of branches labeled $i : 1$. Each of these branches consists of solutions with i identical drops (of zero width at $L = L^\star$) and one different drop (of width $L^\star$ at $L = L^\star$) and no dry spots; as one traverses the curve labeled $i : 1$ the zero width drops gradually grow and become identical to the original drop at $L = (i + 1)L^\star$, where the $i : 1$ branch terminates on the $i + 1$ primary branch. In addition each singular point $L = nL^\star$, $n = 1, 2, \ldots$, generates an uncountable number of solution branches consisting of solutions *with* dry spots (not shown), and these fill the region in Fig. 4 above the no-dry-spot solutions just described. The accessible areas for these solutions

can be constructed in a straightforward way. First one constructs n-drop branches with inner symmetries by assuming that i identical drops with $w < L^\star$ are combined with $j = n-i$ identical drops with $w > L^\star$. This allows for a unique solution with $j(V(w_j) - w_j) = -i(V(w_i) - w_i)$. Calculating w_j for all $0 \le w_i \le L^\star$ gives the $i : j$ branch connecting the singular points on the $n = j$ and $n = i + j$ primary branches, respectively. The area accessible to general n-drop solutions lies between all the $1 : j$ branches ($1 \le j \le n-1$) and the $n-1 : 1$ branch. Fig. 4 shows all the n-drop branches with inner symmetries for $n \le 5$.

The large degree of degeneracy exhibited by this problem is a consequence of the absence of interaction between drops separated by dry spots. This in turn is a consequence of our idealized formulation of the problem. As is well known, the degeneracy can be lifted by incorporating microscopic physics, such as fluid–substrate interactions, into the formulation of the problem. However, as discussed next, the degeneracy is also lifted when the film is placed on an inclined substrate. In the absence of disjoining pressure or contact line pinning by microscopic heterogeneities all solutions 'slide' as soon as the substrate is inclined, and dry spots are no longer possible. Thus for nonzero inclination α, however small, all drops communicate via ultrathin inter-drop films, and coarsening transitions can proceed. This is the subject of the remainder of the present paper. The plethora of sliding solutions identified in the next section for small values of α is of course an echo of the degeneracy of the $\alpha = 0$ case.

4. The inclined substrate

4.1. Weakly nonlinear theory

When $\alpha > 0$ finite wavelength instabilities of the flat film are generically associated with Hopf bifurcations. These lead to traveling waves, i.e., structures that slide down the substrate [31]. In a periodic domain of period L these occur at

$$Ma = Ma_n \equiv Ma_c\left(1 + \frac{k_n^2}{Bo}\right), \tag{17}$$

where $k_n \equiv 2\pi n/L$, $n = 1, 2, \ldots$. The associated frequencies are $\omega_{n0} = \alpha k_n$. Near each of these bifurcations we can use perturbation theory to determine the direction of branching of the resulting traveling waves, as well as their speed.

We write $h(x,t) = 1 + \epsilon\delta(\xi)$, where $\xi = x - vt$, and integrate the resulting equation once:

$$\begin{aligned}\frac{1}{3\,Bo}\delta_{\xi\xi\xi} + \left(\overline{Ma} - \frac{1}{3}\right)\delta_x + \alpha\delta \\ = v(\epsilon)\delta + K(\epsilon) + \epsilon\left(-\frac{1}{Bo}\delta\delta_{\xi\xi\xi} - \alpha\delta^2 + A\delta\delta_\xi\right) \\ +\epsilon^2\left(-\frac{1}{Bo}\delta^2\delta_{\xi\xi\xi} - \frac{1}{3}\alpha\delta^3 + B\delta^2\delta_\xi\right).\end{aligned} \tag{18}$$

Here $K(\epsilon)$ is a constant of integration determined by the requirement $\int_0^L \delta\,\mathrm{d}x = 0$, and

$$\begin{aligned}&\overline{Ma} \equiv \frac{1}{2}\frac{Ma\,Bi}{(1+Bi)^2}, \qquad A \equiv 1 - \frac{2\overline{Ma}_n}{1+Bi}, \\ &B \equiv 1 - \frac{1-2Bi}{(1+Bi)^2}\overline{Ma}_n.\end{aligned} \tag{19}$$

Thus

$$\overline{Ma}_n = \frac{1}{3}\left(1 + \frac{k_n^2}{Bo}\right). \tag{20}$$

To solve Eq. (18) we write

$$\begin{aligned}\delta(\epsilon) &= \delta_0 + \epsilon\delta_1 + \epsilon^2\delta_2 + \cdots, \\ v(\epsilon) &= v_0 + \epsilon v_1 + \epsilon^2 v_2 + \cdots, \\ K(\epsilon) &= K_0 + \epsilon K_1 + \epsilon^2 K_2 + \cdots,\end{aligned} \tag{21}$$

and define the small parameter ϵ using

$$\overline{Ma} = \overline{Ma}_n + \epsilon^2\mu_2. \tag{22}$$

Thus $\mu_2 = \mathrm{O}(1)$ measures (for each n) the distance from the nth Hopf bifurcation. At O(1) we now find that $\delta_0 = a\sin k_n\xi$, $v_0 = \alpha$, $K_0 = 0$ and recover the threshold (20). At $\mathrm{O}(\epsilon)$ the solvability conditions, that is, the conditions guaranteeing that δ_1 is a periodic function of x, imply that $v_1 = 0$, $K_1 = \alpha a^2/2$, and hence that

$$\delta_1 = b_1\cos 2k_n\xi - c_1\sin 2k_n\xi, \tag{23}$$

where

$$b_1 \equiv \frac{1}{4}\left(1 + \frac{Bo\,A}{k_n^2}\right)a^2, \qquad c_1 \equiv \frac{Bo}{4k_n^3}\alpha a^2. \tag{24}$$

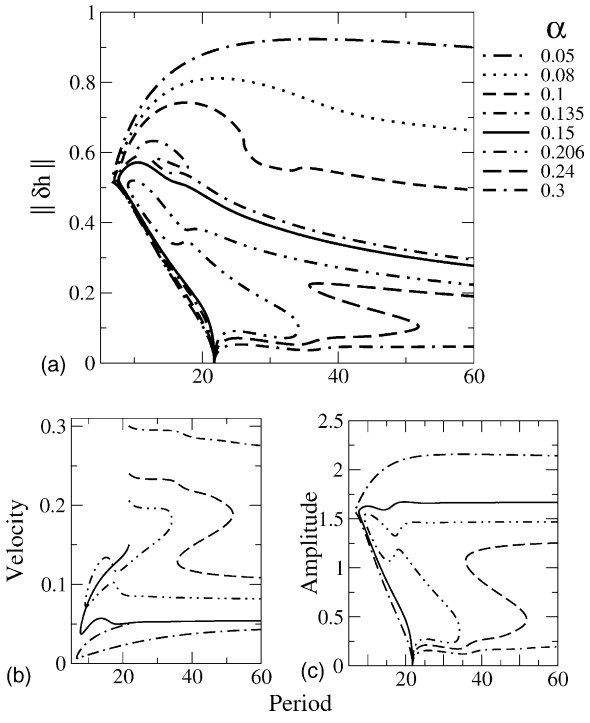

Fig. 8. Traveling wave solutions of Eq. (1) along the $n = 1$ primary branch as a function of L when $Ma = 3.5$, $Bi = 0.5$ and $Bo = 0.5$. (a) The L_2 norm of $\delta h \equiv h(x) - 1$ for different values of the inclination α. (b) The corresponding drift velocity v. (c) The amplitude $\Delta h \equiv h_{\max} - h_{\min}$. The linestyles in (b) and (c) correspond to those used in (a). The saddle-node departs from its location at $L \approx L^\star$ once $\alpha > 0.2$.

The corresponding solvability conditions at $O(\epsilon^2)$ give the desired results:

$$\mu_2 = -\left[\frac{1+4Bi+6Bi^2}{12(1+Bi)^2} + \frac{1}{72}\left(\frac{1+3Bi}{1+Bi}\right)^2 \times \left(1+\frac{Bo}{k_n^2}\right)\right]\left(1+\frac{k_n^2}{Bo}\right)a^2 + \frac{\alpha^2\, Bo}{4k_n^4}a^2, \tag{25}$$

$$v_2 = -\frac{\alpha}{8(1+Bi)}\left[5+7Bi+(1+3Bi)\frac{Bo}{k_n^2}\right]a^2. \tag{26}$$

Thus for small inclinations α the bifurcation is always *subcritical*, cf. Figs. 2 and 8, while for sufficiently large inclinations the bifurcation is always *supercritical*, regardless of n. For $n = 1$ the transition from subcritical to supercritical occurs at $\alpha \equiv \alpha_1 = 0.168$, in agreement with Fig. 9, box 5. In all cases the nonlinearity *reduces* the speed of the traveling wave.

In the following we choose instead to fix the value of $\overline{Ma}$ ($>1/3$) and vary the spatial period L to allow longer and longer wavelength disturbances. In this case instability sets in at $L_n \equiv 2\pi n[Bo(3\overline{Ma}-1)]^{1/2}$ and if we write

$$L = L_n + \epsilon^2 v_2, \tag{27}$$

we find that

$$v_2 = \frac{1}{8(1+Bi)^2}\frac{\overline{Ma}_n}{3\overline{Ma}_n - 1}[2(1+4Bi+6Bi^2) - (7+30Bi+45Bi^2)\overline{Ma}_n]a^2 + \frac{\alpha^2}{4Bo}\frac{a^2}{(3\overline{Ma}_n-1)^2}, \tag{28}$$

$$v_2 = -\frac{\alpha}{8(1+Bi)}\left[5+7Bi+\frac{1+3Bi}{3\overline{Ma}_n-1}\right]a^2. \tag{29}$$

These results enable us to plot the loci of $\mu_2 = 0$ in the (α, Bi) plane for different values of the spatial period, as well as the loci of $v_2 = 0$ for different values of Ma. These plots provide a great deal of information about the small amplitude behavior of the system.

Like the small amplitude states all larger amplitude nonuniform solutions of Eq. (6) drift downstream. Such solutions rapidly become non-sinusoidal. The simplest ones of this type are stationary in reference frames moving with constant speed and satisfy the equation

$$Q(h)\left(\alpha + \left(\frac{h_{xx}}{Bo} - \partial_h f(h)\right)_x\right) - vh + C_0 = 0, \tag{30}$$

where v is the downstream velocity in the laboratory frame. Here x denotes the comoving variable $x + vt$, and C_0 is a constant of integration that, in contrast to the reflection-symmetric case $\alpha = 0$, cannot be set to zero. The constant C_0 may be identified with the flux of liquid in the comoving system. We choose

$$C_0 = \Gamma_0 + vh_0 \equiv -Q(h_0)\alpha + vh_0 \tag{31}$$

corresponding to a uniform film of thickness h_0. The corresponding flux in the laboratory frame is then given by $\Gamma_0 = -Q(h_0)\alpha$. Note that for a given value

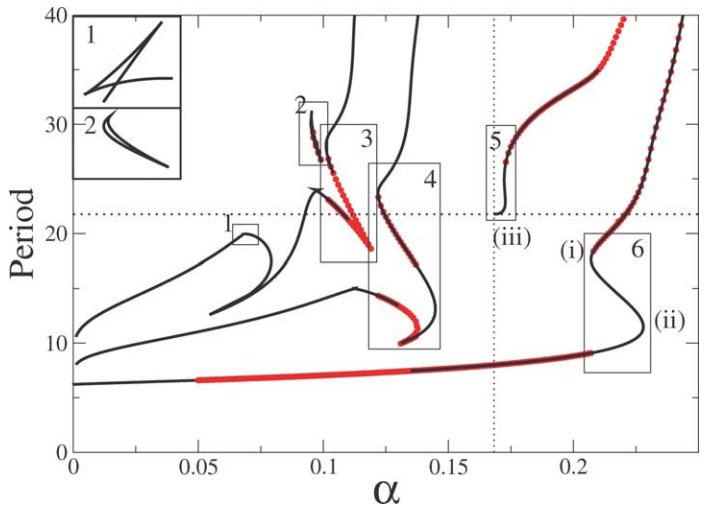

Fig. 9. The loci of saddle-node bifurcations on the $n = 1$ branches in the (α, L) plane (solid black lines) obtained by continuation for $Ma = 3.5$, $Bi = 0.5$ and $Bo = 0.5$. The decoration by the dots indicates saddle-nodes on the primary $n = 1$ branch; the remainder are on secondary branches. The events marked (i)–(iii) indicate the creation and annihilation of pairs of saddle-nodes, and the emission of a saddle-node from the primary bifurcation of the flat state, respectively. The boxes 1–6 frame sequences of transitions discussed in the text. The horizontal dotted line indicates the critical period $2\pi/k_c$ for the linear stability of the flat film (Eq. (4)), while the vertical dotted line indicates the transition between sub- and supercritical bifurcation as obtained from weakly nonlinear theory in Section 4.1 (Eq. (25)). The insets show a 30×60 enlargement of box 1, and a 6×1 enlargement of box 2.

of Γ_0, i.e., of h_0, there may be two homogeneous solutions with this flux, $h = h_0$ and $h = h_0'$, where

$$h_0' = h_0 \left(-\frac{1}{2} + \sqrt{\frac{3v}{\alpha h_0^2} - \frac{3}{4}} \right). \tag{32}$$

The second solution is therefore present whenever $v/\alpha h_0^2 > 1/3$, and corresponds to the so-called conjugate solution, as discussed in the falling film context, for instance, in [44,45]. The lengths h_0' and h_0 appear in the profile of drops of large volume, with h_0' corresponding to the thickness in the plateau region between adjacent drops, and h_0 characterizing the thickness of the plateau region within the drop (see below). Continuity between the cases $\alpha = 0$ and $\alpha \neq 0$ demands that as $\alpha \to 0$ these lengths converge to the ones already identified for $\alpha = 0$, i.e., to the fixed points of Eq. (10). These are 0 and h_{crit} given by Eq. (13). These results can be used to calculate the velocity of long drops in the limiting case of vanishing inclination,

$$\lim_{\alpha \to 0} \frac{v}{\alpha} = \frac{h_{\mathrm{crit}}^2}{3}. \tag{33}$$

In [27,39] a similar problem is discussed in connection with the transition between dewetting on a horizontal plane and sliding drops on an inclined plane.

The selection problem for $\alpha = 0$ discussed in Section 3 is resolved *dynamically* once the substrate is inclined. The only "dry spot" solutions that can move without involving divergencies at the contact line are the ones with zero microscopic contact angle, i.e., the ones on the thick dashed line in Fig. 2. It is therefore not surprising that the stationary solutions of Eqs. (30) and (31) with periodic boundary conditions reproduce, for very small values of α, the thick (and thick dashed) curves of Fig. 2. However, the "dry spots" on the upper (thick dashed) branch are no longer dry, and instead adjacent "drops" are separated by a very thin film, of thickness of order 10^{-5} for $\alpha = 0.001$. The resulting drop solution slides downslope with a very small velocity ($v \approx 10^{-5}$). The appearance of such ultrathin films can be viewed as dynamic generation of precursor films similar to those invoked on horizontal substrates to permit contact line motion, or simply as a dynamic effect: the moving drops leave behind them a thin film, and in a periodic array there is no

'first' drop. However, as discussed below, the stability of the resulting configuration is another matter, and depends on the relevant timescales for the movement of the drops and any instability of the ultrathin film, as well as on the distance between adjacent drops. In the following section we examine the properties of this type of solution in greater detail.

4.2. Stationary solutions and their linear stability

In this section we study in detail the various possible spatially periodic uniformly traveling solutions of Eqs. (30) and (31) together with their linear stability properties. We do this using continuation [21] either in the period L or the amplitude Δh, starting from small amplitude solutions obtained as neutrally stable solutions of the linearized problem, i.e., sinusoidal solutions with period $L_c = 2\pi/k_c$, where k_c is given by Eq. (4). We emphasize, however, that on the real line all perturbations with $0 < k < k_c$, i.e., $L > L_c$, grow in time. We may start from a solution consisting of just one period L_c or from a 'replicated' solution with period nL_c, where n is an integer. We call the resulting solution branches emanating from the zero amplitude state (the uniform film) n-mode primary branches. Branches bifurcating from these in secondary bifurcations will be called secondary solution branches. The $n > 1$ primary branches can be obtained directly from the $n = 1$ branch by multiplying the solution period by n. Solutions on such branches have "internal symmetry" Z_n, in addition to the SO(2) symmetry due to translation invariance of the system. The secondary bifurcations either respect the discrete Z_n symmetry (in which case they correspond to saddle-node bifurcations) or break it, creating a secondary branch of lower symmetry.

The continuation yields a family of stationary nonlinear solutions we call $h_0(x)$; these solve the nonlinear eigenvalue problem for the speed v specified by Eqs. (30) and (31), subject to periodic boundary conditions with spatial period L. To determine the stability of these solutions we write $h(x) = h_0(x) + \epsilon h_1(x)\,e^{\beta t}$, where h_1 is an infinitesimal perturbation *in the comoving frame*. Eq. (6), linearized in ϵ, yields an eigenvalue problem for the growth rate, β, and the associated eigenfunction, $h_1(x)$:

$$\begin{aligned}\beta h_1 = &\left\{\left[Q_h\left(h_{0x}f_{hh} - \frac{h_{0xxx}}{Bo}\right)\right]_x + (Qh_{0x}f_{hhh})_x\right\}h_1 \\ &+ \left[2Qh_{0x}f_{hhh} + Q_h\left(2h_{0x}f_{hh} - \frac{h_{0xxx}}{Bo}\right)\right]h_{1x} \\ &+ Qf_{hh}h_{1xx} - \frac{Q_h h_{0x}h_{1xxx}}{Bo} - \frac{Qh_{1xxxx}}{Bo} \\ &- (\alpha Q_h h_1)_x + vh_{1x}, \end{aligned} \tag{34}$$

where all derivatives of f are functions of the stationary profile $h_0(x)$ and $Q = h_0(x)^3/3$.

The eigenvalues and eigenfunctions of this problem are obtained using a three step procedure. First, h_0 is determined using numerical continuation techniques [21] starting from analytically known small amplitude solutions as described in [27]. Second, the eigenvalue problem is discretized in space and solved numerically. The necessary equidistant discretization imposes a strong limitation on the parameter range where it can be used. The method gives, for instance, no reliable eigenvalues for large periods or step profiles. To avoid this problem we employ a third step, using the results for small periods as starting solutions for numerical continuation in L of the solution of the nonlinear eigenvalue problem (30) together with the linear eigenvalue problem (34). This extended system consists of 11 first-order differential equations (3 for h_0 and 8 for the real and imaginary parts of h_1). Using this procedure we can calculate both h_0 and h_1 and the associated eigenvalues v and β in parallel, for any system parameters. Moreover, points of special interest, such as the location of zero or maximum growth rate, or of the transition between real and complex eigenvalues, can also be followed through parameter space. This procedure works not only for the primary solution branches but also for *secondary* branches, for reasons explained in Appendix A.

4.2.1. The $n = 1$ primary branch

We start by studying the primary branch for $n = 1$ as a function of α. In Fig. 8(a) we show the RMS amplitude $\|\delta h\| \equiv \sqrt{\int_0^L (h - \bar{h})^2\,\mathrm{d}x/L}$ along this branch as a function of the imposed spatial period L for several values of the inclination α computed for

$Ma = 3.5$, $Bi = 0.5$ and $Bo = 0.5$. The figure retains the qualitative properties of the nucleation and drop solutions found for $\alpha = 0$ (see Figs. 2 and 4). Specifically, the subcritical small amplitude nucleation solutions present for $\alpha = 0$ persist for sufficiently small α, together with a vestige of the cusp at $L \approx L^\star$ with which they terminate when $\alpha = 0$. Likewise, the large amplitude "drop" solutions persist, but with one important difference: these solutions contain no dry spots, and $h_{\min}$ is strictly positive, albeit very small. However, the figure also shows that with increasing α the primary branch changes its shape dramatically. First, the amplitude of the drop-like solutions decreases, while at the same time their downstream velocity increases (Fig. 8(b)). This is not surprising: as α increases the film flows faster, and hence for a fixed prescribed flux in the laboratory frame the film thickness must be less. Fig. 8(c) shows these results in terms of the amplitude $\Delta h \equiv h_{\max} - h_{\min}$, and shows that asymptotically all these solutions become independent of L. However, the fact that the decrease in amplitude is ultimately nonmonotonic (at fixed L) indicates that rather more must be happening in the nonlinear regime. This new behavior comes in through a hysteresis bifurcation that introduces a pair of saddle-node bifurcations on the upper part of the branch. Parts of the branch then pinch off yielding isolated loops or *isolas* of solutions. At the same time the primary bifurcation changes from subcritical to supercritical. From Fig. 8(a) it is difficult to infer how exactly the saddle-nodes appear. To understand this process better we follow in Fig. 9 the loci of the saddle-nodes in Fig. 8(a) as a function of α. Note that only the parts decorated by the dots correspond to the branches shown in Fig. 8; the remainder lie on branches that are not connected to the trivial (flat) state. Fig. 10 provides a more complete picture of the evolution of the primary branch with α, as well as including other $n = 1$ branches (dashed and dotted lines) produced via secondary bifurcations from $n > 1$ primary branches. The latter are omitted from Fig. 8(a) for the sake of clarity.

In Fig. 9 different types of codimension-two bifurcations can be seen:

(i) Creation of a pair of saddle-nodes.
(ii) Annihilation of a pair of saddle-nodes.
(iii) Emission of a saddle-node from the primary bifurcation on the flat film solution (i.e., a transition from sub- to supercritical branching).

Annihilation or creation of saddle-nodes can occur with or without a change in the number of branches. The possible processes are most easily described in

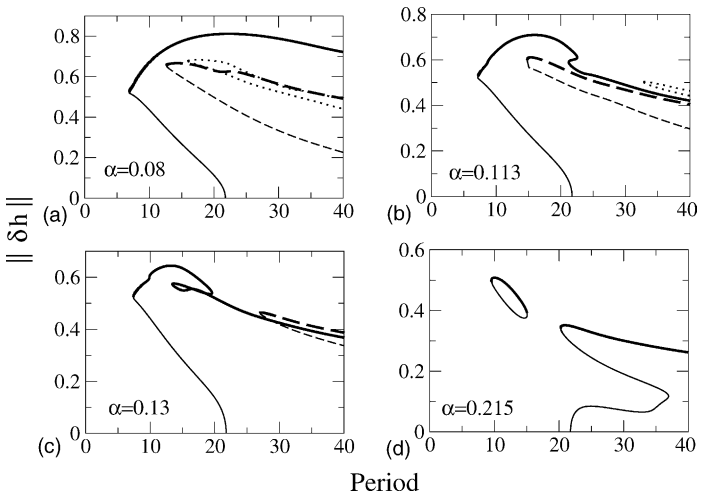

Fig. 10. The L_2 norm $\|\delta h\|$ as a function of L along the primary (solid lines) and different secondary (dashed and dotted lines) $n = 1$ branches for several values of α and $Ma = 3.5$, $Bi = 0.5$ and $Bo = 0.5$. Note the appearance of a hysteresis bifurcation between (a) and (b) and a reconnection of the primary and secondary branches between (b) and (c). In (d) the primary branch is supercritical, and an isola is present. Heavy lines indicate drop-like solutions.

terms of the corresponding normal forms for an amplitude a. We write these in terms of a distinguished bifurcation parameter λ and an unfolding parameter ϵ. The possible processes are:

(a) a hysteresis bifurcation, described by the normal form

$$\lambda + \epsilon a - a^3 = 0, \tag{35}$$

(b) the destruction or creation of a loop, described by the normal form

$$a^2 + \lambda^2 - \epsilon = 0, \tag{36}$$

and (c) a 'necking' bifurcation resulting in reconnection of existing branches, described by the normal form

$$a^2 - \lambda^2 + \epsilon = 0. \tag{37}$$

In (a) when $\epsilon < 0$ there are no saddle-node bifurcations on $a(\lambda)$; the branch develops an inflection point, $\mathrm{d}^2\lambda/\mathrm{d}a^2 = 0$ at $\epsilon = 0$, and two saddle-node bifurcations for $\epsilon > 0$. In contrast, in (b) solutions only exist in the interval $-\sqrt{\epsilon} < \lambda < \sqrt{\epsilon}$ and form a closed loop that shrinks to nothing as ϵ decreases to zero. In (c) when $\epsilon < 0$ the solutions form two hyperbolas $a = \pm\sqrt{\lambda^2 - \epsilon}$ separated by $2\sqrt{-\epsilon}$ in a. When $\epsilon = 0$ the two hyperbolas pinch together at the origin forming two straight lines, $a = \pm\lambda$. For $\epsilon > 0$ these reconnect forming two hyperbolas separated by $2\sqrt{\epsilon}$ in λ and introducing two saddle-node bifurcations. For more details see [46].

The boxes in Fig. 9 frame particularly interesting transitions that make use of these elementary processes. We describe these from left to right, i.e., for α increasing:

1. A secondary branch develops a pair of additional saddle-nodes below the original one in a hysteresis bifurcation. The upper two then annihilate in a (reverse) hysteresis bifurcation, resulting in an overall decrease in the amplitude at the 'nose'. This sequence of transitions corresponds to a quartic fold, with the normal form $a^4 - \lambda + \epsilon_1 a + \epsilon_2 a^2 = 0$ [46], and is responsible for the presence of the structure shown in the inset. This structure is a consequence of a projection of the two parameter unfolding in (ϵ_1, ϵ_2) onto a single unfolding parameter ϵ in Fig. 9. The same structure is present at the vertex of the neighboring curve (corresponding to a different secondary branch), just below box 2.
2. A hysteresis bifurcation creates a saddle-node pair which is then destroyed in another hysteresis bifurcation, creating a closed loop of saddle-node loci (see enlargement of box 2 in Fig. 9).
3. A necking bifurcation between the primary and one of the secondary $n = 1$ branches at $L \approx 28$ creates another pair of saddle-node bifurcations, followed by the annihilation at $L \approx 18$ of one of these with the saddle-node at the 'nose' of the original secondary $n = 1$ branch (a hysteresis bifurcation). This 'reconnection' between the primary and secondary $n = 1$ branches thus changes the large L behavior of the primary branch, with the thick solid curve in Fig. 10(b) becoming a thick dashed curve in Fig. 10(c) and vice versa. The remaining saddle-node created in the necking bifurcation moves to $L = \infty$ prior to the hysteresis bifurcation. This corresponds to the disappearance of the dotted branch in Fig. 10(b).
4. Here the first bifurcation is again a necking bifurcation, but this time it switches the termination of the primary branch to a *different* $n > 1$ branch than before (cf. the solid and dashed curves in Fig. 10(b) and (c)). This transition is followed by a hysteresis bifurcation on the primary branch at small L, followed by a reverse necking bifurcation that detaches an isola of solutions from the 'crest' of the primary branch (cf. Fig. 10(c)). Before this loop shrinks to zero the large L saddle-node (and the whole of the dashed branch in Fig. 10(c)) moves off to infinity. Thus only one saddle-node (the 'nose' on the primary branch) remains for α on the right boundary of box 4.
5. A saddle-node is emitted from the primary bifurcation at $L = L_c$ when $\alpha_1 \approx 0.168$ (dotted line) as predicted by the weakly nonlinear theory in Section 4.1. At this point the primary bifurcation changes from subcritical to supercritical (cf. Fig. 10(c) and (d)). This event is followed by the creation of an isola of solutions to the right of this

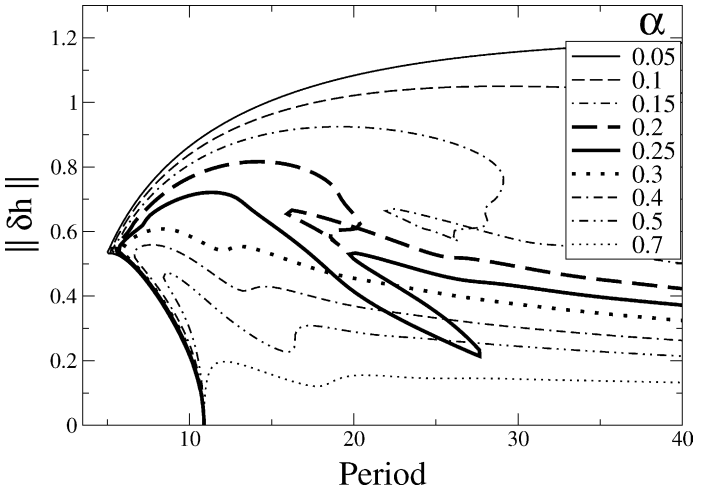

Fig. 11. Same as Fig. 8(a) but for $Ma = 5.0$.

saddle-node, which reconnects with the primary branch as α increases, thereby annihilating two of the saddle-nodes.

6. The 'nose' on the primary branch pinches off at $L \approx 18$ via a necking bifurcation and the resulting isola shrinks and vanishes with increasing α. The net effect is to shift the 'nose' to the right (cf. Fig. 10(d)).

For larger values of Ma the behavior becomes yet more complicated, as illustrated in Fig. 11 for $Ma = 5.0$. We do not discuss here the details of the transitions indicated by this figure, except to point out that the saddle-node bifurcation on the primary $n = 1$ branch departs from $L = L^\star$ once α exceeds $\alpha \approx 0.4$. This value should be compared with $\alpha = 0.2$ for a similar effect at $Ma = 3.5$.

4.2.2. Linear stability of the $n = 1$ branch

Fig. 12(a) summarizes the linear stability results along the $n = 1$ primary branch when $Ma = 3.5$, $Bi = 0.5$, $Bo = 0.5$ and $\alpha = 0.135$: the broken heavy lines indicate intervals of stability. All of these lie on the upper part of the branch and hence correspond to drop-like states. These results are obtained for perturbations of the same wavelength L as the basic state $h_0(x)$, i.e., instability with respect to longer wavelengths (coarsening) is not indicated. Such longer wavelength perturbations are considered when performing the stability analysis of the $n > 1$ primary branches. Some of the $n > 1$ primary branches are also shown. The proximity of these branches to the $n = 1$ branch may be responsible for some of the

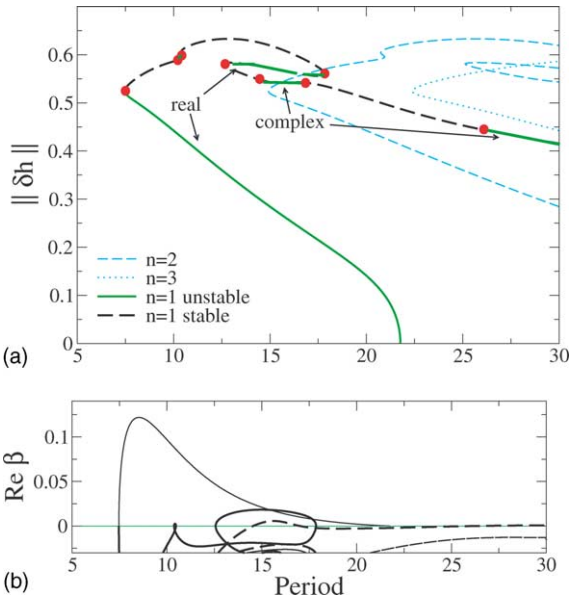

Fig. 12. (a) The stability properties of the primary $n = 1$ branch with respect to perturbations of period L when $Ma = 3.5$, $Bi = 0.5$, $Bo = 0.5$ and $\alpha = 0.135$. Solid (dashed) lines represent unstable (stable) solutions. (b) Largest eigenvalues β along the upper (thick lines) and lower (thin lines) parts of the primary $n = 1$ branch. Solid (dashed) lines represent real (real part of a complex pair of) eigenvalues. The solid black dots in (a) indicate the location of secondary steady state and Hopf bifurcations.

complexity revealed by the stability analysis (see below).

Because the $n = 1$ primary branch bifurcates subcritically from the linearly stable flat film solution the branch is initially linearly unstable, and remains so until the saddle-node bifurcation at which the branch turns towards larger L. As already explained, this bifurcation is located near $L = L^\star$, and signals the transition from nucleation solutions to drop-like solutions. Thus the drop-like solutions are initially stable. Fig. 12 shows that for $Ma = 3.5$ and $\alpha = 0.135$ this bifurcation occurs at $L \approx 8$ ($L^\star = 6.2$) and corresponds to a real eigenvalue passing through zero. In Fig. 12(b) the leading real eigenvalue along the branch of drop-like solutions is indicated by a heavy line, and one sees that this eigenvalue goes through two successive loops within which it in fact becomes positive. These loops are responsible for the pairs of saddle-node bifurcations visible in the bifurcation diagram shown in Fig. 12(a). Fig. 12(b) also shows the complex eigenvalues (dashed lines), and shows that the same complex eigenvalue is responsible for the three successive Hopf bifurcations indicated in Fig. 12(a). Note, in particular, the presence of back-to-back Hopf bifurcations that introduce an instability 'bubble' between $L \approx 14$ and 17.

Fig. 13 compares the unstable eigenfunctions $h_1(x)$ with the corresponding profiles $h_0(x)$ at four locations along the primary branch. Fig. 13(a) shows $h_0(x)$ and $h_1(x)$ at $L = 10$ along the lower (nucleation) branch. The solution $h_0(x)$ reveals an incipient 'hole' at which the unstable eigenfunction is largely localized. Fig. 13(b) and (c) shows the corresponding results for $L = 15$ in the two unstable intervals along

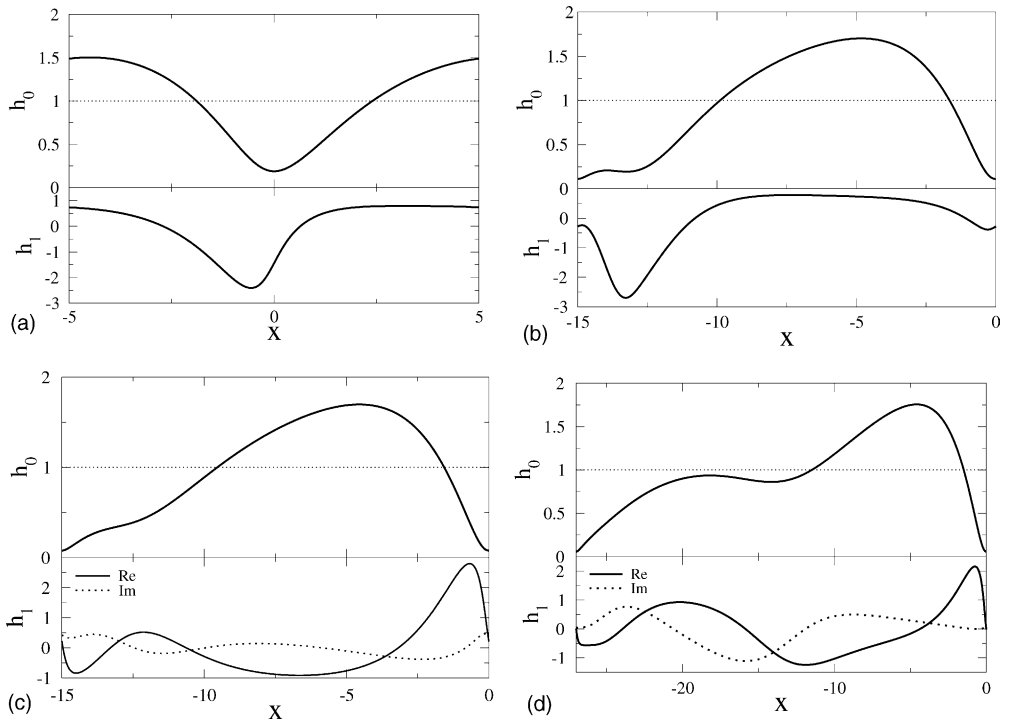

Fig. 13. A comparison between the solutions $h_0(x)$ and the unstable eigenfunctions $h_1(x)$ at several different locations along the primary $n = 1$ branch for the parameters of Fig. 12. (a) $L = 10$, (b) $L = 15$ (upper unstable interval), (c) $L = 15$ (middle unstable interval), and (d) $L = 27$. Note that the steady state instability ((a) and (b)) is localized in the hole region of each solution, while the oscillatory instability ((c) and (d)) has largest amplitude at the front of the drop. The sign of the eigenfunctions h_1 is arbitrary but their amplitude is normalized such that $\|h_1\| = 1$; in (c) and (d) the solid and dotted lines show the real and imaginary parts of the eigenfunction $h_1(x, t)$ at a particular instant in time.

the upper branch. The basic state in the first of these (the 'upper' unstable interval) has a more pronounced 'hole' as expected for a solution on the drop-like part of the primary branch, with the unstable eigenfunction localized at the front of the drop (at the right of the figure), and even more strongly at the inflection point at the back of the drop. These facts suggest that the hysteresis in this part of the primary $n = 1$ branch is in fact due to an incipient instability attempting to introduce a second droplet into the solution. We believe that the proximity of the $n = 2$ primary branch (labeled $n = 2$ in Fig. 12(b)) to this hysteresis loop supports this interpretation of the unstable eigenfunction. The results shown in Fig. 13(c) are for the unstable solution on the lower part of this hysteresis loop. The unstable eigenvalue is now complex (see Fig. 12(b)) but the unstable eigenfunction remains localized at the front and back of the drop. However, this time the largest oscillation amplitude is found at the front of the drop, indicating that the instability can be associated with an oscillatory instability of the front. As L increases the drop develops a longer and longer plateau of thickness $h \approx 1$ (Fig. 13(d) for $L = 27$) but the oscillatory instability remains associated with the front of the drop, with a much broader and smaller maximum amplitude associated with its back (Fig. 13(d)). Note, however, that since $Ma > Ma_c$ the plateau region must itself be unstable, and Fig. 13(d) shows that this is indeed so.

4.2.3. Connection with the $\alpha = 0$ solutions

It is of interest to understand how the structure of $h_0(x)$ shown in Fig. 13 is connected to the nucleation and drop solutions obtained for $\alpha = 0$. To this end we return to Fig. 10(a) with $\alpha = 0.08$, and plot the solutions $h_0(x)$ at selected points along the upper (thick continuous line) and lower (thin continuous line) segments of the $n = 1$ branch, and compare these with solutions along the upper (thick dashed line) and lower (thin dashed line) part of the secondary branch also included in the figure. The latter is strongly subcritical and does not connect to any of the primary branches with $n \leq 4$. For this value of α the saddle-node on the $n = 1$ branch is located at $L \approx 6.9$. Fig. 14(a) shows that for L not too large ($L = 10$) the upper branch solutions do indeed resemble the drop solutions with zero contact angle present for $\alpha = 0$. The figure also shows that with increasing L (e.g., $L = 40$) these solutions become markedly asymmetrical but still retain their drop-like appearance. Note, in particular, the gradual development of a narrow undershoot in the profile marking the front of the drop. This is the thinnest part of the film, and indicates where any rupture may be expected to occur. The adjacent phase plane projections show that this overshoot is associated with the appearance of a complex (spatial) eigenvalue of a fixed point $h_x = h_{xx} = h_{xxx} = 0$ of Eq. (30) written as a dynamical system in the spatial variable x. The figure also shows that the solutions on the secondary branch are dominated by the $n = 1$ solution, although they also contain an admixture of $n = 2$. With increasing L the thin plateau region disappears, but the thinnest part of the film remains associated with the front of the drop and comparable in magnitude to that along the primary $n = 1$ branch. These conclusions apply to the other secondary branches that are present in this region (see Fig. 10(a)) as well. Fig. 14(b) shows the corresponding results for $\alpha = 0.113$ for which the saddle-node on the primary $n = 1$ branch occurs at $L = 7.2$. The behavior of $h_0(x)$ with increasing L is qualitatively the same, except that the longer drops now develop a plateau with $h_0 \approx 1$, much as seen for $\alpha = 0.135$.

The development of asymmetry is seen most clearly in the comoving streamlines shown in Fig. 15. For example, Fig. 15(a) shows the result for $\alpha = 0.08$, $L = 10$. The drop is sliding towards the right with speed $v = 0.021$. This motion has almost no effect on the drop shape which resembles that for $\alpha = 0$ (cf. Fig. 7) but the streamlines are already markedly asymmetric. As discussed further below this is a consequence of the fact that films on a substantially inclined substrate are described well by the Kuramoto–Sivashinsky equation which possesses an unphysical reflection symmetry at leading order that is broken only at higher order. However, as seen from Eq. (15) this symmetry is absent from the equations for the streamlines. Fig. 15(b) shows the corresponding result for $\alpha = 0.08$, $L = 40$. Since the drop is heavier it slides faster ($v = 0.053$) and its profile becomes markedly asymmetric. The front counterclockwise cell is greatly compressed

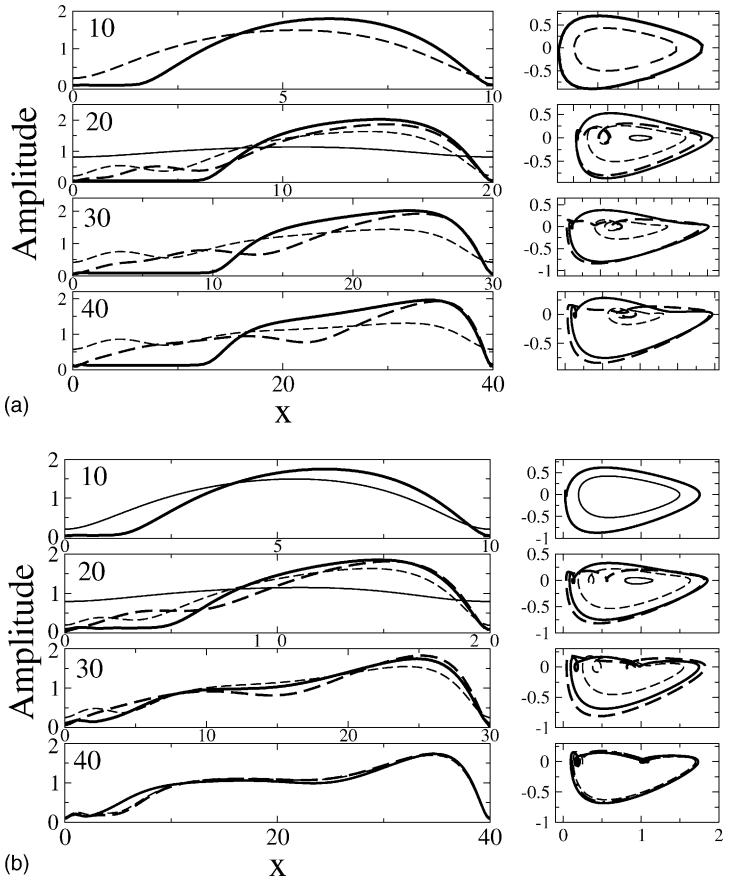

Fig. 14. Profiles of primary (solid lines) and secondary (dashed lines) $n = 1$ solutions for $Ma = 3.5$, $Bi = 0.5$, $Bo = 0.5$ and different periods L when (a) $\alpha = 0.08$, (b) $\alpha = 0.113$. Thick (thin) lines refer to upper (lower) parts of each branch as in Fig. 10. Note the asymmetry in the profiles and the development of an extended 'dry' spot as L increases. The solutions in (b) develop an undershoot just before the front of the drop; this undershoot manifests itself as a small spiral in the (h, h_x) phase portraits shown in the right set of panels. The secondary solutions along the dotted branch in Fig. 10 are not shown.

while the back clockwise cell now occupies most of the drop volume. At the same time the 'hole' becomes shallower, permitting the presence of an open streamline which enters the drop from the right, hugs its front as the ambient fluid is swept into it before being expelled along the bottom. In Fig. 15(c) for $\alpha = 0.215$, $L = 35$ the long plateau region is responsible for the appearance of a *pair* of additional clockwise cells, separated from the original clockwise cell (and from one another) by stagnation points. The drop slides quite rapidly ($v = 0.09$) and does so on top of a slower film attached to the substrate. The volume of fluid trapped within the drop (rather than circulating through it) is smaller and decreases to zero as the inclination α increases. Fig. 15(d) shows an example for $\alpha = 0.215$, $L = 25$ containing no closed streamlines. This pattern is characteristic of a traveling surface wave; the phase velocity of this wave is 10 times larger than the sliding speed of the drop in Fig. 15(a).

4.2.4. The $n = 2$ primary and secondary branches

As already mentioned the primary branches with $n > 1$ consist of n *identical* waves or drops, and hence are susceptible to secondary bifurcations that break the discrete internal translational symmetry that results. Such bifurcations result in a longer spa-

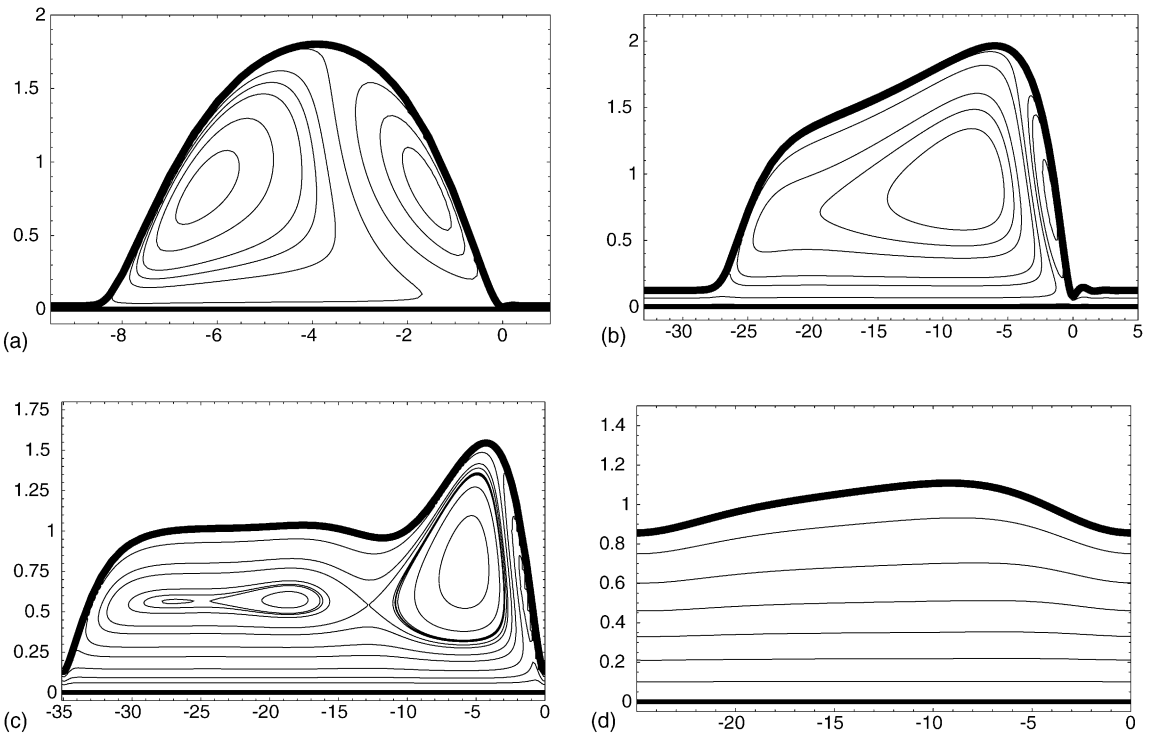

Fig. 15. Comoving streamlines for different inclination angles and periods when $Ma = 3.5$, $Bi = 0.5$ and $Bo = 0.5$. (a) $\alpha = 0.08$, $L = 10$, $v = 0.021$, with $\psi = 0.015, 0.01, 0.004, -0.001, -0.005, -0.0075, -0.01, -0.015, -0.02$; (b) $\alpha = 0.08$, $L = 40$, $v = 0.053$, with $\psi = 0.015, 0.01, 0.005, -0.001, -0.0035, -0.0075, -0.01, -0.015, -0.0175, -0.02$; (c) $\alpha = 0.215$, $L = 35$, $v = 0.09$, with $\psi = -0.005, -0.0075, -0.011, -0.015, -0.0175, -0.02, -0.02199, -0.022, -0.0222, -0.02227, -0.0225, -0.025, -0.03$; (d) $\alpha = 0.215$, $L = 25$, $v = 0.21$, with $\psi = -0.02, -0.04, -0.06, -0.08, -0.1, -0.12, -0.14$. The last panel shows a solution on the small amplitude surface wave branch formed when the primary bifurcation becomes supercritical.

tial period and hence are associated with coarsening of the pattern. They are familiar from earlier analyses of both the Eckhaus instability [47], and of the Kuramoto–Sivashinsky equation [20].

Fig. 16 shows the $n = 2$ primary branch (solid black line) for several different values of the slope α. Qualitatively, the evolution of this branch follows that found already for the $n = 1$ primary branch (see Figs. 8 and 10). In particular the primary bifurcation again becomes supercritical for sufficiently large α. Fig. 16 also shows a number of secondary branches (dashed black lines) that bifurcate from the $n = 2$ branch. Some of these reach large values of L and may go off to infinity (as happens in the Rayleigh–Bénard problem at large Prandtl numbers), while others reconnect to the $n = 2$ branch. Remarkably, none actually connect to the $n = 1$ primary branch, although there is no reason why such a connection should not occur. These secondary branches all consist of two-humped solutions but with no symmetry between the humps, although near the secondary bifurcation that produces them the bumps are of course almost identical. This is seen clearly in Fig. 17 which shows the profiles at selected points along both the $n = 2$ primary branch and the secondary branches that bifurcate from it when $\alpha = 0.2$, ordered from top to bottom according to the distance to the secondary bifurcations along the branch. Each panel in this figure refers to a different branch in Fig. 16(b), with (a) referring to the primary $n = 2$ branch, and (b)–(f) referring to the secondary branches bifurcating from the $n = 2$ branch at locations indicated by solid dots in Fig. 16(b), starting with the first of these at $L \approx 43$ (Fig. 17(b)) and following up the $n = 2$ branch. The last two secondary branches lie es-

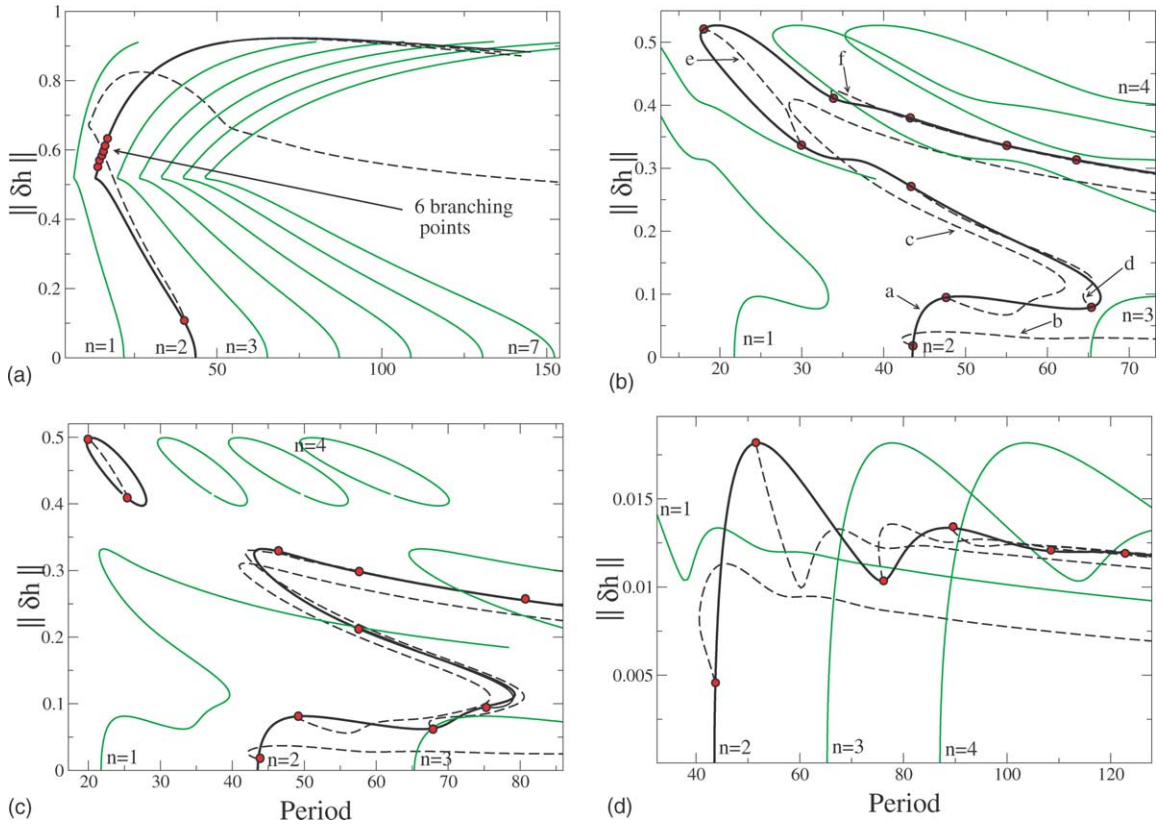

Fig. 16. The $n = 2$ primary (solid dark lines) and secondary (dashed dark lines) branches for $Ma = 3.5$, $Bi = 0.5$, $Bo = 0.5$ and (a) $\alpha = 0.05$, (b) $\alpha = 0.2$, (c) $\alpha = 0.22$, (d) $\alpha = 0.8$. The other primary branches are shown in gray. Secondary bifurcations on the $n = 2$ primary branch are indicated by solid black dots. The letters in panel (b) indicate the secondary branches corresponding to the respective panels of Fig. 17 showing film thickness profiles.

sentially on top of the $n = 2$ branch (and so are invisible in Fig. 16(b)) and are omitted. In the phase space projection shown in the rightmost panels the bifurcations to the secondary branches correspond to (spatial) period-doubling. Fig. 18 shows the slide speed v along each of these branches. Since the solutions resemble the $n = 2$ solutions their speed is almost identical to that along the $n = 2$ primary branch. Moreover, the amplitude $\Delta h \equiv h_{\max} - h_{\min}$ for these solutions also becomes independent of L when L is large. Fig. 18 shows that v generally decreases with L towards an asymptotic value $v_\infty > 0$, as a result of the increasing wavelength of the solution, and we expect this to be so even in Fig. 18(a) for large enough L.

We remark that Fig. 16(d) for $\alpha = 0.8$ is of the type familiar from studies of falling films [1] and indeed the Kuramoto–Sivashinsky equation. This result suggests that the new behavior we have described here occurs for very shallow inclinations of the substrate only, with a quite abrupt change in behavior for larger inclinations (for fixed *Ma*, *Bi*, *Bo*), despite the fact that our model equation does not include effects of inertia. A similar simplification occurs for small *Bo* (at fixed *Ma*, *Bi*, α). In both these regimes the bifurcation structure becomes almost independent of the values of the fixed parameters.

4.2.5. *Linear stability of $n = 2$ primary branch*

Fig. 19 shows the dominant eigenvalues along the $n = 2$ branch when $\alpha = 0.135$ (shown dashed in Fig. 12). In this figure the gray lines (solid indicating real eigenvalues, dashed indicating the real part

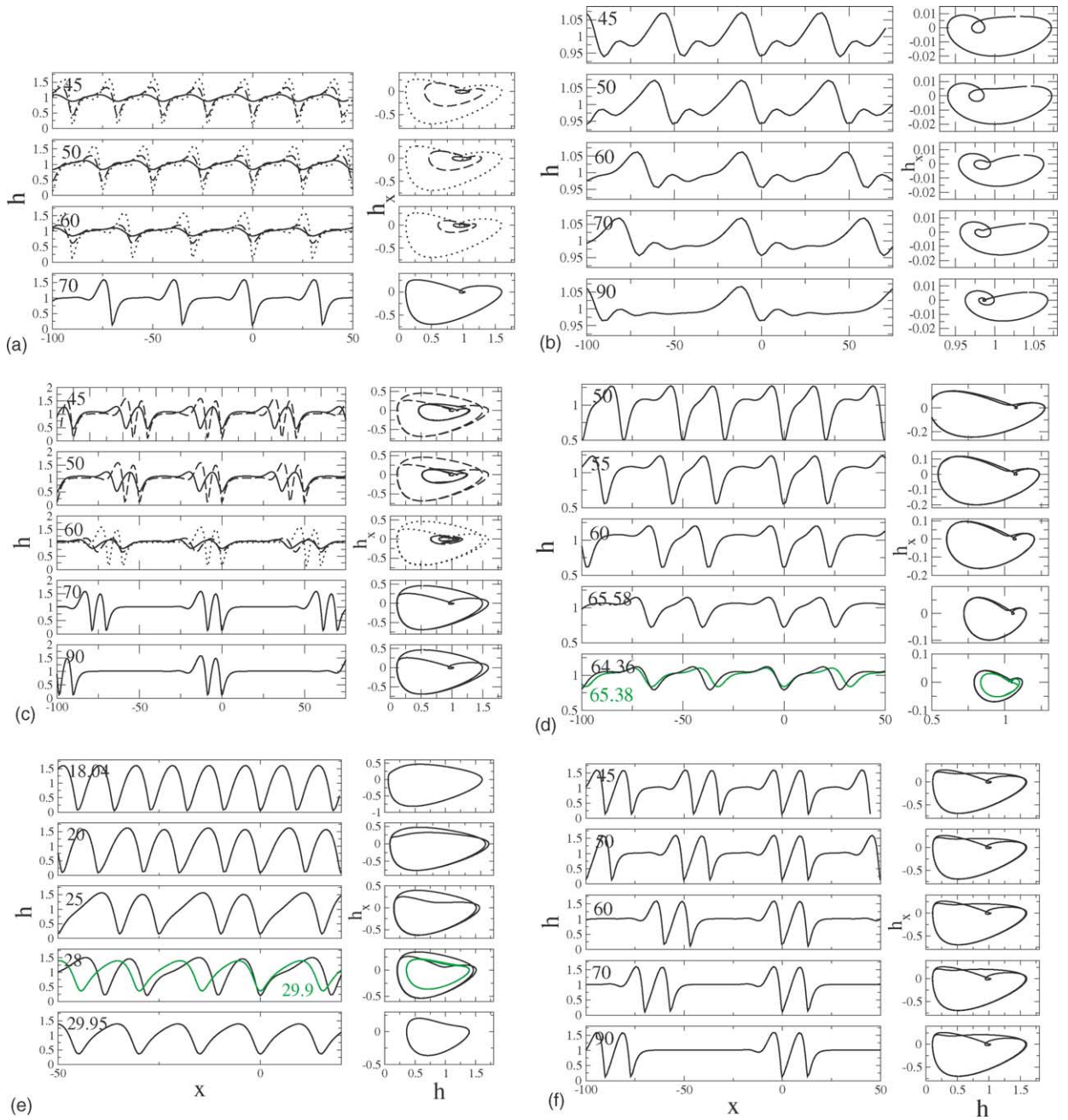

Fig. 17. Film thickness profiles along the $n = 2$ primary branch (panel (a)) and the $n = 2$ secondary branches (panels (b)–(f)) when $Ma = 3.5$, $Bi = 0.5$, $Bo = 0.5$ and $\alpha = 0.2$ for different periods as given in the legends. The respective branches are indicated in Fig. 16(b) by the corresponding letter. In cases where a given value of L cuts a branch in several locations the solid line refers to the upper solution, dashed to the middle and the dotted to the lowest.

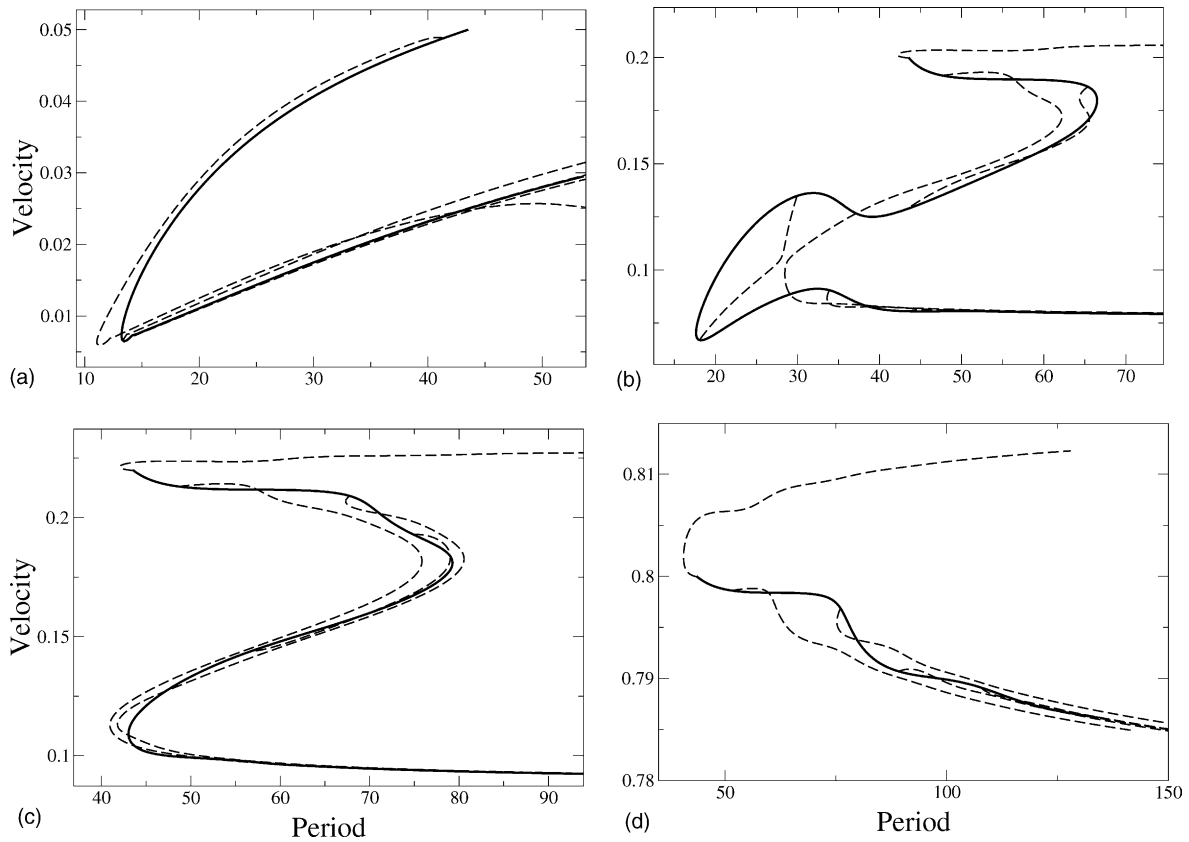

Fig. 18. The drift velocity v along the $n = 2$ primary (solid lines) and secondary (dashed lines) branches for (a) $\alpha = 0.05$, (b) $\alpha = 0.2$, (c) $\alpha = 0.22$, (d) $\alpha = 0.8$ and the parameters of Fig. 16.

of a complex pair) show the eigenvalues that preserve the internal symmetry of the solution, i.e., eigenvalues whose eigenvectors lie in the fixed point subspace of this symmetry. Thus, for example, the location where the solid gray line passes through $Re\,\beta = 0$ near $L \approx 15$ corresponds to the saddle-node bifurcation on the $n = 2$ branch. The black lines (solid indicating real eigenvalues, dashed indicating the real part of a complex pair) indicate eigenvalues whose eigenvectors break this internal symmetry. Such bifurcations correspond to the development of asymmetry between the two drops. Fig. 19(a) shows the eigenvalues along the upper part of the branch (above the saddle-node) while Fig. 19(b) shows the eigenvalues along the lower part. The latter is unstable with two unstable eigenvalues, one corresponding to a symmetric eigenvector which passes through zero at the saddle-node, and the other corresponding to an antisymmetric one which only stabilizes above the saddle-node (see inset), producing a short interval of stability on the upper part of the branch ($15.2 < L < 19$) terminated by a Hopf bifurcation producing symmetric oscillations (cf. Fig. 19(a)). There are other stable intervals as well. It is of interest to mention that the primary symmetric eigenvector is obtained from the $n = 1$ via the replication procedure, while the antisymmetric eigenvector is there *because* the $n = 2$ branch bifurcates *after* the $n = 1$ branch. Fig. 19 also indicates the presence of intervals in L in which the $n = 1$ and the $n = 2$ branches are *both* unstable. This fact is of interest since in this interval the solutions must have a more complicated time-dependence than a simple traveling wave, cf. [48].

The corresponding results for $\alpha = 0.2$ are shown in Fig. 20. This figure shows the leading eigenvalues

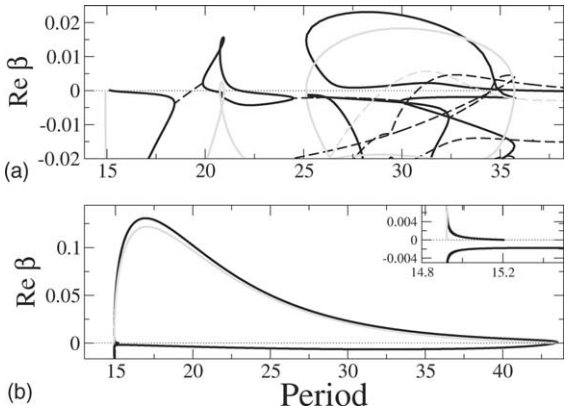

Fig. 19. The dominant eigenvalues β along the $n = 2$ primary branch for $Ma = 3.5$, $Bi = 0.5$, $Bo = 0.5$ and $\alpha = 0.135$ (shown as a gray dashed line in Fig. 12). The solid (dashed) lines indicate real (complex) eigenvalues. The gray (black) lines refer to symmetry-preserving (-breaking) perturbations. Panel (a) refers to the upper part of the branch, while (b) refers to the lower part, above and below the saddle-node bifurcation at $L \approx 14.92$, respectively.

along the top, middle and lower portions of the $n = 2$ primary branch shown in Fig. 16(b). From Fig. 20(c) we see that there is a stable interval between $L \approx 47.5$ and $L \approx 51$ on the lower part of the branch, while Fig. 20(a) shows that there is another stable interval on the upper part between $L \approx 18$ and $L \approx 27$. The part of the branch between the two saddle-nodes is, as usual, unstable throughout (Fig. 20(b)). In both cases stability is acquired at a steady state bifurcation, the second secondary bifurcation in the former case, and the left-most saddle-node bifurcation in the latter. Moreover, in both cases the branch subsequently loses stability via a Hopf bifurcation. The corresponding results for $\alpha = 0.8$ are shown in Fig. 21. The primary $n = 2$ branch is now supercritical and there are no

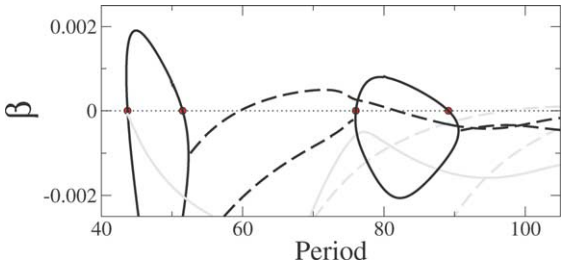

Fig. 21. The real parts of the largest eigenvalues β along the $n = 2$ primary branch when $Ma = 3.5$, $Bi = 0.5$, $Bo = 0.5$ and $\alpha = 0.8$ (Fig. 16(d)) showing intervals of stability in $51 < L < 60$ and $89 < L < 97$. The solid (dashed) lines indicate real (complex) eigenvalues. The gray (black) lines refer to symmetry-preserving (-breaking) perturbations.

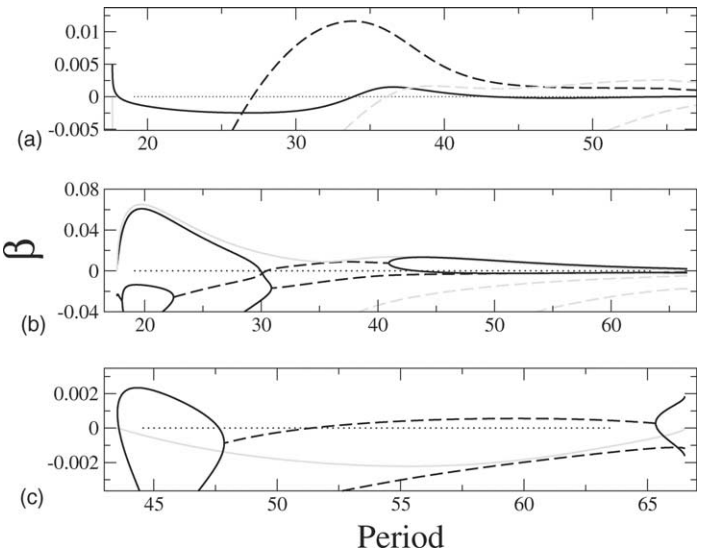

Fig. 20. The real parts of the largest eigenvalues β along the $n = 2$ primary branch when $Ma = 3.5$, $Bi = 0.5$, $Bo = 0.5$ and $\alpha = 0.2$. Panels (a)–(c) refer to the upper, middle and lower parts of the branch. The solid (dashed) lines indicate real (complex) eigenvalues. The gray (black) lines refer to symmetry-preserving (-breaking) perturbations. The figure reveals intervals of stability on both the lower and upper parts. The part between the two saddle-nodes (Fig. 16(b)) is unstable everywhere.

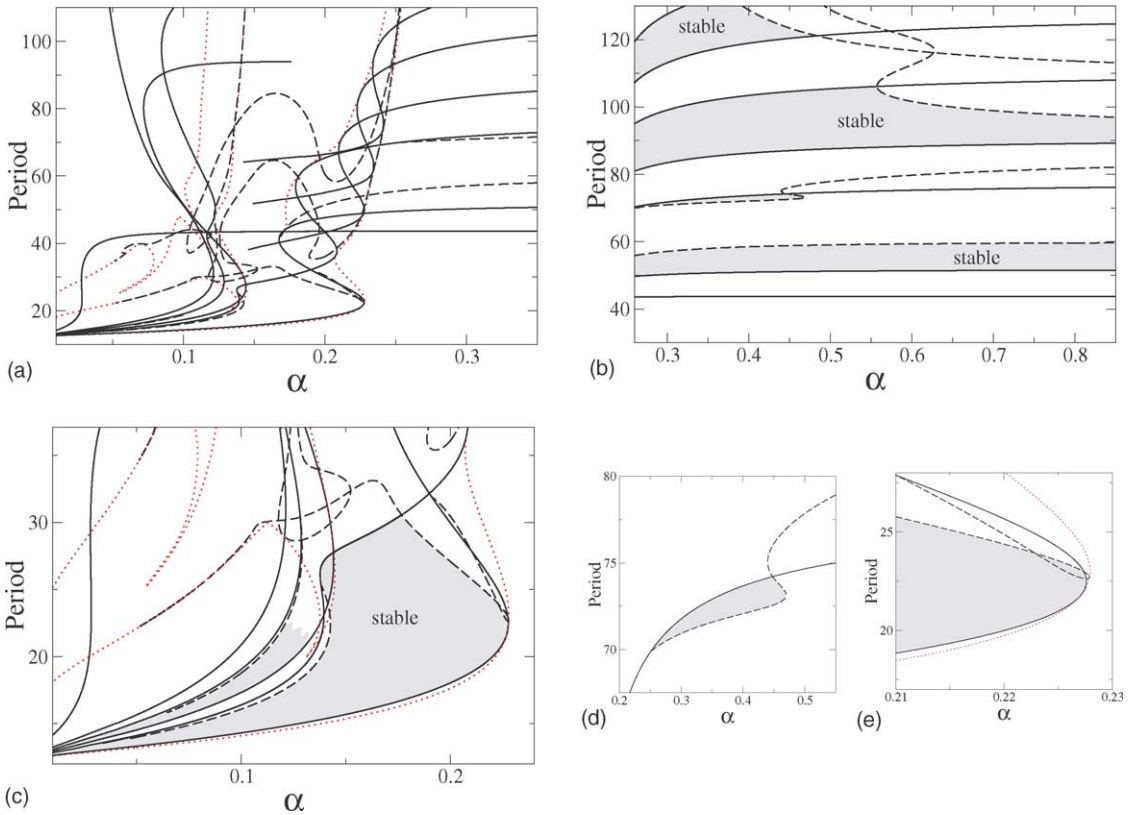

Fig. 22. Loci of bifurcation points on the $n = 2$ primary branch as a function of the inclination α for $Ma = 3.5$, $Bo = 0.5$ and $Bi = 0.5$. The solid (dashed) lines represent steady state (Hopf) bifurcations. The dotted lines denote the saddle-nodes already shown in Fig. 9 but scaled for the $n = 2$ branch. Panel (a) shows the transition between the small and large α regimes, while (b) and (c) show the large and small α regime, respectively. Regions where the primary $n = 2$ branch is linearly stable are shaded gray. Only the first two bands of stable solutions are indicated. The shading of the second band is discontinued near the necking bifurcation (see text), which reorders the branches. The enlargement (d) shows a region where a Takens–Bogdanov bifurcation is present while (e) zooms in on the disappearance of an isola.

saddle-node bifurcations. The figure shows that there are two intervals in L within which the $n = 2$ branch is stable, located approximately in $51 < L < 60$, and $89 < L < 97$.

Fig. 22(a) summarizes these results in a different way. The figure shows the loci of saddle-node (dotted lines), steady state (solid lines) and Hopf (dashed lines) bifurcations in the (α, L) plane, and highlights the fact that for small α ($\alpha < 0.1$) as well as for large α ($\alpha > 0.26$) the behavior of the system simplifies dramatically, with very intricate behavior in the transition region in between. There one can distinguish two subregions: (i) the behavior in $0.1 < \alpha < 0.15$, reflecting the complexity associated with the reconnections between primary and secondary branches (boxes 3 and 4 in Fig. 9), and (ii) the behavior in $0.17 < \alpha < 0.25$, resulting from the transition from sub- and supercritical primary bifurcation (box 5 in Fig. 9) responsible for the formation of a small amplitude portion of the primary branch with solutions in the form of surface waves. The figure represents the bifurcations without indicating on which portion of the branch they may occur; thus a particular bifurcation can move from one portion of the branch to another (for example, from the nucleation or lower portion to the drop-like upper portion) as one traverses the bifurcation locus. For instance, the S-shaped curves describing the steady state bifurcations around $\alpha = 0.2$ describe pairs of steady

state bifurcations that emerge from the saddle-node between the surface wave and nucleation portions of the branch, one onto each portion. With increasing α one bifurcation moves along the nucleation branch segment towards smaller periods and annihilates at the "nose" with a bifurcation approaching along the large amplitude portion. The behavior is even more involved around $\alpha = 0.12$ where bifurcations can also change between primary and secondary branches. The superposition of results for different branches is responsible for the crossing of the different curves. Note, that some curves in Fig. 22(a) are not shown in their entirety, and hence are absent from some of the enlargements. These represent bifurcation points on secondary branches that are not considered further.

The most accessible regime, the surface waves for larger α, is shown in Fig. 22(b). Here the primary branch is supercritical and consists of surface waves only. There are no saddle-node bifurcations. Consequently one can readily identify the different bifurcations and the bands of linearly stable solutions (indicated by shading) already discussed for $\alpha = 0.8$ (Fig. 21). As one approaches $\alpha \approx 0.25$ from above stable bands with larger and larger periods are added.

The behavior for small α is shown in Fig. 22(c). For very small α the branching points cluster around the saddle-node bifurcation at the 'nose' separating the nucleation and large amplitude drop-like branches, and approach the singular point at period L^* as $\alpha \to 0$. Using Figs. 19(a) and 20(a) one can easily identify the first stable region on the large amplitude branch segment (indicated by gray shading in Fig. 22(c)). However, Fig. 19(a) reveals a second stable band as well, present for $L > 22$ and ending at the next saddle-node at $L \approx 36$. The situation is complicated by the fact that the large amplitude portion of the branch may undergo further saddle-node bifurcations, as is the case, for example, when $\alpha = 0.135$. In Fig. 22(c) this second band is also shaded gray, but the shading is discontinued at the location of the necking bifurcations involving disconnected branches, cf. Fig. 10.

Finally, the figure also indicates the presence of Takens–Bogdanov bifurcations, where the Hopf frequency vanishes. Such bifurcations mark the endpoints of the dashed curves (Hopf bifurcations) on solid curves denoting saddle-node bifurcations, for example, at $\alpha \approx 0.191$ and $\alpha \approx 0.138$ (Fig. 22(c)) and at $\alpha \approx 0.26$ (on the left boundary of Fig. 22(b), shown in detail in Fig. 22(d)). Of course in the laboratory frame these bifurcations are responsible for the introduction of a *second* frequency into the dynamics of the system. Finally, Fig. 22(e) shows a detail of the region where the large isola shown in Fig. 16(c) vanishes.

4.2.6. *Primary branches with $n > 2$*

The branching behavior associated with subsequent primary branches becomes ever more complex. In Fig. 23(a) we show the branching associated with $n = 4$ (black lines) with an enlargement included in Fig. 23(b), both for $\alpha = 0.8$, together with some of the secondary branches originating from the $n = 2$ branch (dashed gray lines) and indeed the other primary branches (continuous gray lines). In this figure the solid black line represents the $n = 4$ primary branch, the long-dashed black lines represent secondary branches that bifurcate from it, while the short-dashed lines represent tertiary branches, i.e., branches that bifurcate from the secondary branches.

The main purpose of Fig. 23 is, once again, to demonstrate the immense complexity in solution space of this apparently simple system. All of the solutions shown are steady in an appropriately sliding frame; we do not follow or show oscillatory solutions, even though we have located a number of secondary Hopf bifurcations as well. Of course this complexity grows as α *decreases* because of the extreme degeneracy of the $\alpha = 0$ case described in Section 3 (cf. Fig. 24).

4.2.7. *The small α regime*

We conclude the discussion of the different types of solutions by showing an amplitude-spatial period plot summarizing the primary branches (which are almost independent of the inclination α) and the various secondary branches that connect them, for several values of α near $\alpha = 0$ (Fig. 24). The dot-dashed lines in the figure represent the symmetric multidrop solutions emanating from the singular points $L^\star$ on the primary branches (Fig. 4), while the remaining lines show their analogues for $\alpha > 0$. For $\alpha = 0.005$ and $\alpha = 0.01$ it is still possible to identify the analogues of the 1:1, 1:2

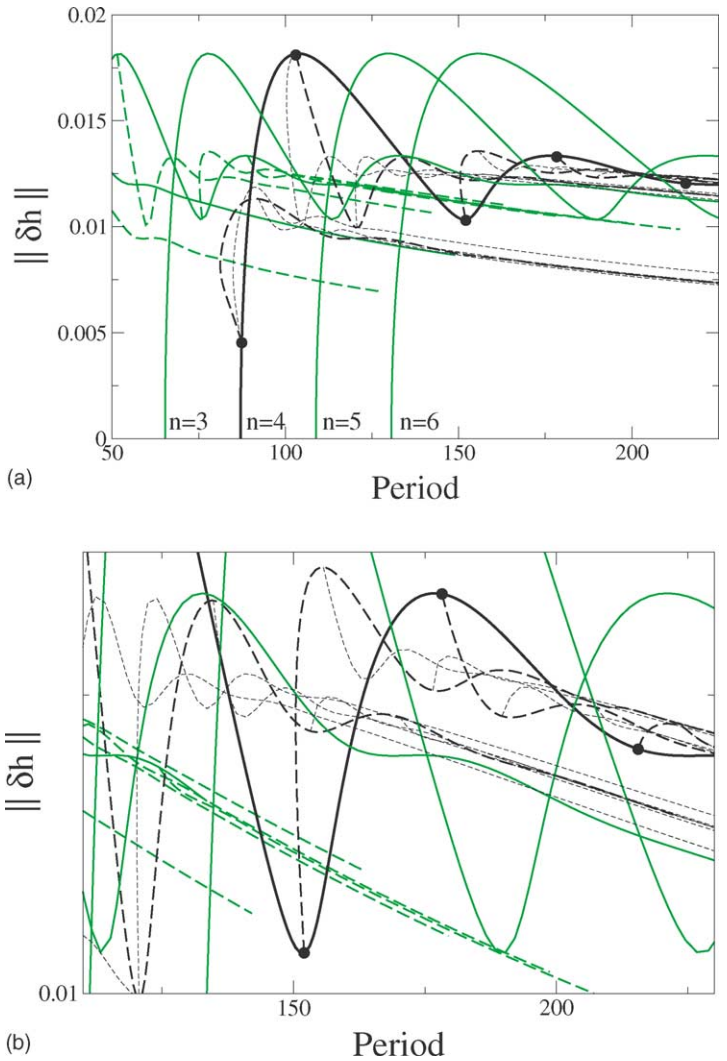

Fig. 23. The $n = 4$ primary (solid black line), secondary (dashed black line) and tertiary (dotted black line) branches for $Ma = 3.5$, $Bi = 0.5$, $Bo = 0.5$ and $\alpha = 0.8$. Solid gray lines show the corresponding $n \neq 4$ primary branches, while dashed gray lines show secondary $n = 2$ branches. Panel (b) shows a detail of (a). Secondary bifurcations are indicated by solid black dots.

and 2:1 branches, even though their end points have shifted away from the points nL^*. The left termination of the 1:1 branch is still on the $n = 2$ primary branch but the 1:2 and 2:1 branches no longer bifurcate from the $n = 3$ branch and are only connected to one another. Thus for $\alpha > 0$ the 1:2 and 2:1 branches disconnect from the $n = 3$ branch, although for small α this fact may be almost invisible (see Fig. 24). In fact the connection between the 1:2 and 2:1 branches remains close to the $n = 3$ branch even for larger α, as these branches gradually transform themselves to a branch of traveling waves. By the time α reaches $\alpha = 0.05$ the bifurcation diagram no longer resembles the $\alpha = 0$ results.

The small α limit is amenable to a theoretical simplification as well. Specifically, if we take $\alpha = \epsilon^3\hat{\alpha}$, and write $h(x, t) = 1 + \epsilon^2\delta(X, T)$, where $X = \epsilon x$, $T = \epsilon^4 t$ are slow variables, we obtain from Eq. (1)

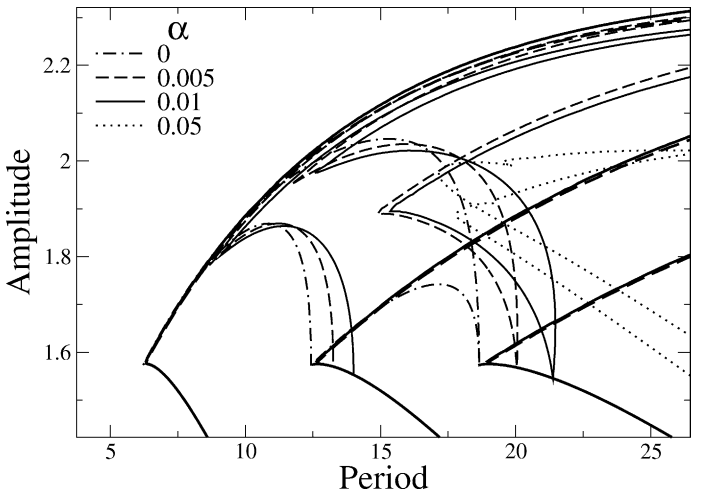

Fig. 24. The dependence of the multidrop branches on the inclination α for comparison with Fig. 4 for $\alpha = 0$ (dashed-dotted). The primary branches are almost independent of α. The multidrop branches appear to emanate from the near-singular point on the $n = 1$ primary branch, provided α remains small. The parameters are $Ma = 3.5$, $Bi = 0.5$, $Bo = 0.5$.

the Childress–Spiegel equation [49] with a drift term:

$$\delta_T - \left(\frac{1+3Bi}{3+3Bi}\right)(\delta\delta_X)_X = -\hat{\alpha}\delta_X - \frac{1}{2}\frac{\mu\, Bi}{(1+Bi)^2}\delta_{XX} - \frac{1}{3Bo}\delta_{XXXX} + O(\epsilon). \tag{38}$$

Here μ is the bifurcation parameter, defined by

$$Ma = Ma_c + \epsilon^2\mu, \tag{39}$$

where Ma_c is given by Eq. (3), and $\delta(x,t)$ is required to have zero mean: $\bar{\delta} = 0$. Thus, whenever $\alpha > 0$ the solutions drift with speed v, and the symmetry of the problem changes from O(2) to SO(2). Weakly nonlinear theory of the type described in Section 4.1 shows (cf. [49]) that with periodic boundary conditions on a domain of length L

$$\mu_2 = -\frac{(1+Bi)^2}{36Bi}\frac{Bo}{k^2}a^2, \qquad v_2 = 0, \tag{40}$$

where we have written $\mu = \mu_c + \epsilon^2\mu_2$, $v = \alpha + \epsilon^2 v_2 + \cdots$. In view of (19) and (22) these results agree with the $k \to 0$ limit of the more general results (25) and (26) when $\alpha = O(\epsilon^3)$. Thus in this limit all primary bifurcations are indeed subcritical.

4.2.8. The large α regime

In contrast, for *large* α, i.e., for physical inclination angles approaching order 1, we write $h = 1 + \epsilon\eta(x - \alpha t, t)$, $\bar{\eta} = 0$, anticipating that the film flows with a speed near α and becomes more and more uniform as α increases. When $\alpha = \tilde{\alpha}/\epsilon$ we find that η satisfies the Kuramoto–Sivashinsky equation

$$\eta_t + 2\tilde{\alpha}\eta\eta_\xi = -\frac{1}{3}\left(\frac{Ma}{Ma_c}\right)\eta_{\xi\xi} - \frac{1}{3Bo}\eta_{\xi\xi\xi\xi} + O(\epsilon), \tag{41}$$

where $\xi \equiv x - \alpha t$. If the higher order terms are neglected the resulting equation has an unexpected symmetry: $\xi \to -\xi$, $\eta \to -\eta$. As a result on a periodic domain the equation possesses O(2) symmetry instead of the expected SO(2) symmetry. This symmetry *forces* all the primary bifurcations to be steady state bifurcations instead of being steady state bifurcations *by accident*. Moreover, all such bifurcations are supercritical [20] in agreement with the conclusion reached in Section 4.1. Of course the Kuramoto–Sivashinsky equation describes only the leading order contribution to the film dynamics, and the inclusion of the $O(\epsilon)$ correction does restore the expected SO(2) symmetry, albeit only in the nonlinear terms. This change of symmetry produces a number

of qualitative changes in the well-known bifurcation diagram for the Kuramoto–Sivashinsky equation [20] by unfolding the secondary bifurcations, much as in [1,50]. As a result the secondary branches may become disconnected from the primary ones. This is the case, for example, for the parity-breaking bifurcation from steady states to traveling waves. In the Kuramoto–Sivashinsky equation with O(2) symmetry this bifurcation is a pitchfork, and the waves can travel in either direction. In contrast, in the presence of small O(2) symmetry-breaking terms the steady states turn into traveling waves, while branches of traveling waves are split into two, since there is now a difference between (nonlinear) waves traveling downstream or upstream (relative to the moving frame). Specifically, the small amplitude part of what was the steady state branch now connects smoothly to the downstream traveling waves created in the original parity breaking bifurcation, while the large amplitude part connects to the upstream branch of traveling waves, and becomes disconnected from the other branch. The drift therefore deforms the original parity-breaking bifurcation into a classic imperfect bifurcation, and this is all that may be expected in such a one-parameter unfolding of a pitchfork bifurcation. In contrast branches of standing waves turn into branches of tori (two-frequency traveling waves) but do *not* become disconnected. Additional observations are made in Ref. [51]. With this in mind the classical analysis of the Kuramoto–Sivashinsky equation with O(2) symmetry provides a good guide to the behavior of our system for sufficiently large α (small ϵ). The consequences of this type of qualitative change are clearly visible in Fig. 16(d), obtained for $\alpha = 0.8$, even though this value of α is *not* large. For larger α the computed diagrams resemble those for the Kuramoto–Sivashinsky equation [20] more and more closely.

5. Discussion

In this paper we have examined in detail the profiles and stability properties of thin films on a horizontal or slightly inclined heated substrate using a model equation incorporating only thermocapillary effects, hydrostatic and Laplace pressure, and gravitational forcing when the substrate is inclined. We focused on a parameter regime in which the film is unstable with respect to long wave thermocapillary modes, avoiding the short wave convective instability [19]. This assumption limits the practical application of our analysis to films that are not too thick (to avoid convection) but not too thin (to justify our omission of van der Waals interaction with the substrate). However, the results provide the basis for understanding the behavior of the system even outside of this regime, for example, with the disjoining pressure included.

Within our formulation we identified two types of solutions, unstable nucleation solutions and stable drop solutions. A careful study of the horizontal substrate problem allowed us to construct a vast family of drop solutions separated by ‘dry’ regions of different lengths. All of these solutions are nominally stable since our formulation does not include any nonhydrodynamic interactions among drops separated by dry regions. Of these solutions those with zero microscopic angle are energetically favored, and form a special class because they can move without involving divergencies at the contact line. We showed, by solving a nonlinear eigenvalue problem, that on a slightly inclined plane periodic drop solutions do indeed slide down the plane, and explored in detail their relationship to the solutions on the horizontal substrate. In particular we showed that on an inclined substrate the dry regions between the drops are replaced by an ultrathin film that enables neighboring drops to communicate. This communication in turn allows coarsening instabilities to proceed, instabilities that do not occur in our model on a horizontal substrate. We concluded that the degeneracy of the horizontal case is responsible for the plethora of solutions present for small inclinations, and determined in some detail(!) the transitions among these as a function of the inclination angle and the spatial period.

Throughout we formulated the problem as one with periodic boundary conditions on a line, and examined the sequence of transitions as the spatial period L increases. For small enough L a given film is stable, but as L increases it undergoes a sequence of bifurcations each of which produces a branch of nonuniform

solutions. Our calculations reveal that these primary bifurcations are typically subcritical, at least for sufficiently small inclinations α, and therefore produce unstable states. We have identified these states with the spatially periodic nucleation solutions. As a result the solutions that are of physical interest are those on the upper branch, above the saddle-node bifurcations at which the primary branches turn around. These saddle-node bifurcations are vestiges of a singularity in the $\alpha = 0$ case at which the minimum thickness of the nucleation solutions vanishes. The reason for this singularity is simple to understand—it is a consequence of the fact that a film of a fixed volume (or spatial period) cannot have an arbitrarily large amplitude without rupture. Beyond this singularity amplitude (i.e., maximum thickness) can only increase at the expense of introducing dry spots into the film structure. Thus when $\alpha = 0$ these larger amplitude solutions are nothing but arrays of drops held together by surface tension, and separated by dry spots. Because of the enormous degeneracy of solutions of this type when $\alpha = 0$ there is a very large number of slowly drifting drop-like states once $\alpha > 0$, and it is these states that constitute the potentially stable solutions above the saddle-node bifurcations. In this regime we have located intervals in the spatial period L containing no stable simple traveling wave solutions. Here one expects states with complex time-dependence, but perhaps more than that, since the profusion of unstable states suggests that the system may wander among these states, exhibiting very long transients even when stable states are available. This type of scenario resembles that discussed recently by Schmiegel and Eckhardt [52,53] in the context of the transition to turbulence in plane Couette flow. At larger α the drift associated with finite inclination starts to dominate the dynamics, and the primary branches become supercritical with the resulting solutions resembling the traveling wavetrains familiar from the Kuramoto–Sivashinsky equation. We have seen that these solutions are in fact connected to the unstable nucleation solutions present for $\alpha = 0$. In this regime chaotic dynamics are still present but the number of unstable solutions is much smaller, a fact that is reflected in shorter transients. Moreover, the chaotic behavior can now be associated with global bifurcations in the phase space of the system.

Our main conclusion, beyond the remarkable richness of this apparently very simple problem, is that the degeneracy of the horizontal case influences the inclined problem only for quite small values of the inclination angle, specifically $\alpha \ll h_0/\ell \sim h_0(\sigma_0/\rho g)^{-1/2}$. For larger inclinations the system behaves much more like the falling films under the influence of inertia studied, for example, in [12,15] even though our theory does not retain inertial effects and the dominant balance in the direction normal to the substrate is still hydrostatic. We showed that such films behave much like the Kuramoto–Sivashinsky equation, and our work can be viewed as a quantification of the range of applicability of this equation to thin films on an inclined plane. Refs. [54,55] show that the approach proposed here remains valuable even for systems with broken translation symmetry. This symmetry can be broken, for example, by inhomogeneous heating, a problem studied recently in the context of a falling film with inertia [56].

As usual in problems of this type the spatial period L is left as a parameter in the theory, although in experiments it may be determined by the fastest growing scale when $Ma > Ma_c$. However, in view of the tendency towards coarsening it is imperative that larger values of L are examined as well. Indeed, it is unlikely that a correct description of systems of this type can be obtained without considering values of L much larger than the wavelength of the primary instability. Our results indicate that this type of problem, like the Kuramoto–Sivashinsky equation, possesses a large variety of solutions in large domains. The result of a simulation may locate a single stable solution, or if it is repeated with different initial conditions, perhaps a different solution. The only way that the results of such simulations can be understood is to focus initially on small periodic domains where the simpler of these solutions first appear, and to trace them to the values of L of interest. This allows one to recognize different solutions, and understand the nature of the transitions among them as L varies. Our results therefore also shed light on the transition to complex spatio-temporal behavior that is characteristic of these systems.

We have shown that unstable modes may be located at the front or the back of the drop, and examined the change in these modes as the volume of the drop increases and it develops an extended plateau region. We did not, however, perform any direct numerical simulations. The main reason is that, for $\alpha = 0$, our model equation is ill-posed, in the sense that it does not possess solutions for all time. Specifically, its solutions cannot be followed past rupture time, when the film thickness first vanishes. This is because as this instant approaches finer and finer scales appear in the problem [57], and these scales becomes infinitely small at the moment of rupture. It is possible that the appearance of smaller scales in the simulation of related equations [7,10] is related to this process, even though of course the equation remains a mathematically acceptable model until rupture time. To our knowledge there are no comparable results for the inclined case, although it is likely that similar results hold. Our approach avoids this issue but also fails to locate time-dependent rupture, and indeed solutions with more complex time-dependence.

Although we are not aware of experiments done on thin liquid films on slightly inclined heated plates, the experimental setups used in the study of the limiting cases of horizontal or vertical plates could easily be adapted for this purpose. The parameters of the system used by VanHook et al. [9] to study the long wave instability on a horizontal heated plate and of a second proposal involving a different silicone oil are tabulated in [10]. For these films the long wave instability remains the dominant instability for films of thickness $h_0 = \mathrm{O}(100\,\mu\mathrm{m})$. For water films, such as those used in [58,59] to study a falling film on a locally heated plate, our model applies for $h_0 \lesssim \mathrm{O}(10\,\mu\mathrm{m})$. However, to model an actual experimental system the influence of the wetting properties of the liquid should be included in the theory via a disjoining pressure. This pressure accounts for the missing interface energy and selects a microscopic contact angle for drops on a horizontal substrate, and hence a unique solution branch from the hatched region in Fig. 2. An attractive interaction between the film and the substrate is likely to have an important effect on the behavior of the film. On the one hand it may stabilize the ultrathin film in the interdrop regions, and increase the range of inclinations for which the large amplitude drop solutions remain stable, thereby shifting the transition between the drop and surface wave regimes towards larger α. On the other hand a strong surface–substrate interaction may also destabilize the ultrathin film in the interdrop region resulting in actual rupture. Should this occur the drops would be unable to slide, and our solutions would become inapplicable. These conjectures are supported by the results of Oron and Bankoff on condensing [60] and evaporating [61] films under the influence of a disjoining pressure.

A related approach for isothermal films with a disjoining pressure also leads to a film equation of the form equation (6) but with a different free energy $f(h)$ [35,39]. The solution of the corresponding time-independent problem for a horizontal plate also yields drops, with drop profiles that have a passing resemblance to those determined here. However, in these drops the liquid is at rest, in contrast to our case in which the surface cooling drives an internal circulation. In this case, too, if the film ruptures the time-dependent thin film equation fails to address the drop selection problem since it breaks down at the precise instant at which the film ruptures. Thus models of this type cannot predict the final equilibrium drop shape when film rupture occurs [62].

Acknowledgements

This work was supported in part by the Deutsche Forschungsgemeinschaft under grant TH781/1 (UT) and by the NASA Microgravity Sciences Program under grant NAG3-2152. We are indebted to A. Bertozzi, M. Bestehorn, J.M. Vega and M.G. Velarde for helpful discussions.

Appendix A. The degeneracy of Eq. (1)

The appearance of Hopf bifurcations once the substrate is inclined is expected on general grounds [31]. However, the way this occurs in Eq. (1) is *non-generic*. This is because the speed with which the resulting waves travel at onset is *independent* of their

wavenumber. This fact is responsible for a number of special features of this equation. These properties are shared by a number of thin film equations but are nongeneric within the larger class of evolution equations. The discussion that follows is crucial for understanding the numerical results reported in Section 4. In particular we explain here why in the present problem secondary branches of solutions consist of single frequency states, when generically in systems with SO(2) symmetry such branches consist of quasiperiodic states. The fact that this is not the case here permits us to compute the secondary states using the same branch following algorithm as used for the primary branches.

We begin with the linear problem in the presence of periodic boundary conditions, and examine solutions growing like $(h(x)-1)\exp st$. In the frame of the substrate, each primary bifurcation is a Hopf bifurcation with frequency $\omega_{n0} = \alpha k_n$, $n = 1, 2, \ldots$. Specifically, the eigenvalue $s_n = \mathrm{i}\alpha k_n$ is associated with the eigenfunction $\exp -\mathrm{i}k_n x$, while the eigenvalue $s_n = -\mathrm{i}\alpha k_n$ is associated with the eigenfunction $\exp \mathrm{i}k_n x$. A traveling wave then takes the form $h(x,t) - 1 = (1/2)[a \exp \mathrm{i}k_n(x-\alpha t) + \bar{a} \exp -\mathrm{i}k_n(x-\alpha t)]$, describing a wave traveling in the $+x$-direction, i.e., downslope. Note that when $\alpha = 0$ the linear problem has a zero eigenvalue of double algebraic multiplicity, i.e., the eigenvalue $s_n = 0$ is associated with two independent eigenfunctions $\exp \pm \mathrm{i}k_n x$. This is a generic feature of problems with O(2) symmetry when the primary instability breaks the symmetry, i.e., $k_n \neq 0$. The resulting bifurcation is a pitchfork of revolution.

In the nonlinear regime the wave frequency depends on the amplitude, as described for example by Eq. (29). Since $\mathrm{d}v_2/\mathrm{d}k_n \neq 0$ the speeds of the different traveling waves differ at finite amplitude. In a reference frame moving with speed α to the right, all the primary bifurcations simultaneously become steady state bifurcations, each associated with a zero eigenvalue of double multiplicity. The corresponding eigenfunctions are $\exp \pm \mathrm{i}k_n x$. However, in this frame the resulting steady solutions begin to drift as soon as their amplitude becomes finite, as described by the normal form

$$\dot{a}_n = \nu a_n + c|a_n|^2 a_n, \tag{A.1}$$

where $c \equiv c_\mathrm{r} + \mathrm{i}c_\mathrm{i}$ is a complex coefficient that depends on n, i.e., the branch of interest. Writing $a_n = R_n \mathrm{e}^{\mathrm{i}\phi_n}$ we have

$$\dot{R}_n = \nu R_n + c_\mathrm{r} R_n^3, \qquad \dot{\phi}_n = c_\mathrm{i} R_n^2. \tag{A.2}$$

Comparing these expressions with those derived in Section 4.1 we deduce that $c_\mathrm{r} = -v_2/a^2$, $c_\mathrm{i} = k_n v_2/a^2$. The frequency of the (nonlinear) traveling waves is therefore given by $\omega_n \equiv k_n(\alpha + v_2 R_n^2)$. The coefficient c_i arises from the term $-\alpha(h^2-1)h_x$ on the right-hand side of Eq. (1) written in the moving frame. This term is the only one that breaks the symmetry $x \to -x$ and it vanishes when $h = 1$ ($\alpha \neq 0$). Thus the linear stability problem in the moving frame is invariant under $x \to -x$ but the nonlinear problem is not.

Since each zero eigenvalue in the moving frame is doubled, the bifurcating branch inherits in general *two* small eigenvalues. As seen from Eq. (A.2) in the case of the $n = 1$ branch one of these eigenvalues is -2ν while the other vanishes. The former describes the stability of the wave with respect to amplitude perturbations and is positive (negative) if the branch bifurcates subcritically (supercritically). The latter describes neutral stability with respect to spatial translations. This pattern repeats for the branches with $n = 2, 3, \ldots$, except of course that the $n = 2$ branch already has two unstable eigenvalues inherited from the $n = 1$ bifurcation that precedes it, and these *may* result in secondary bifurcations on the $n = 2$ branch that involve the $n = 1$ Fourier component. In generic systems with SO(2) symmetry, i.e., spatially periodic systems with broken $x \to -x$ symmetry secondary bifurcations from traveling waves are either saddle-node bifurcations or Hopf bifurcations creating quasiperiodic (two-frequency) states. This is not the case here even though for $\alpha \neq 0$ Eq. (1) also has SO(2) symmetry. To explain why we consider the normal form equations describing the interaction between the $n = 1$ and $n = 2$ bifurcations. Since the corresponding Hopf frequencies are in the ratio 1:2 the appropriate equations (in the moving frame) are

$$\begin{aligned} \dot{a}_1 &= \nu_1 a_1 + d_1 \bar{a}_1 a_2 + (e_1|a_1|^2 + f_1|a_2|^2)a_1 + \cdots, \\ \dot{a}_2 &= \nu_2 a_2 + d_2 a_1^2 + (e_2|a_1|^2 + f_2|a_2|^2)a_2 + \cdots. \end{aligned} \tag{A.3}$$

Equations of this form can be derived from Eq. (1) by a center-unstable manifold reduction of the type described by Armbruster et al. in their study of the Kuramoto–Sivashinsky equation [63]. However, our interest in these equations is not in the coefficients but in the qualitative predictions that can be deduced from them.

We begin by noting that because of the special property of the linear problem both ν_1 and ν_2 are *real*, although all the other coefficients are in general complex. The stability properties of the $n = 2$ solution $(a_1, a_2) = (0, a_{20})$ with respect to perturbations involving the $n = 1$ mode are then given by the solution of

$$\dot{a}_1 = \nu_1 a_1 + d_1 \bar{a}_1 a_{20} + f_1 |a_{20}|^2 a_1. \tag{A.4}$$

The eigenvalues are

$$s_\pm = \nu_1 + f_{1\mathrm{r}} |a_{20}|^2 \pm \sqrt{|d_1|^2 |a_{20}|^2 - f_{1\mathrm{i}}^2 |a_{20}|^4}. \tag{A.5}$$

Thus for small values of $|a_{20}|$, i.e., near the bifurcation to the $n = 2$ state, both of these eigenvalues are *real* and *positive*. As a result the $n = 2$ branch is necessarily doubly unstable at onset (even if it bifurcates supercritically) but can gain stability after two successive steady state bifurcations at which the eigenvalues $s_\pm$ pass through zero. However, because of the nonlinearly induced drift of the state $(0, a_{20})$ the resulting secondary state also drifts downstream, and is therefore a single frequency traveling wave. The drift frequency will, of course, depend on the amplitude of the $n = 1$ contribution to the waveform, and the resulting 'mixed' mode will therefore drift with a different speed than the basic $(0, a_{20})$ state at the same value of the parameters. Single frequency solutions of this type are easily found numerically by solving the appropriate nonlinear eigenvalue problem.

The behavior just described is very different from the generic situation in which the equations in the rest frame of the (zero amplitude) $n = 2$ branch take the form

$$\begin{aligned} \dot{a}_1 &= (\nu_1 + \mathrm{i}\Omega) a_1 + d_1 \bar{a}_1 a_2 \\ &\quad + (e_1 |a_1|^2 + f_1 |a_2|^2) a_1 + \cdots, \\ \dot{a}_2 &= \nu_2 a_2 + d_2 a_1^2 + (e_2 |a_1|^2 + f_2 |a_2|^2) a_2 + \cdots, \end{aligned} \tag{A.6}$$

where $\Omega \equiv \omega_{10} - \omega_{20}/2 \neq 0$. A similar calculation shows that for this case

$$s_\pm = \nu_1 + f_{1\mathrm{r}} |a_{20}|^2 \pm \sqrt{|d_1|^2 |a_{20}|^2 - (\Omega + f_{1\mathrm{i}} |a_{20}|^2)^2}, \tag{A.7}$$

and hence that near onset the two eigenvalues form a *complex* conjugate pair. In this case any secondary bifurcation near onset must be a Hopf bifurcation, and the $n = 2$ state may therefore acquire stability after a *single* secondary Hopf bifurcation. This bifurcation introduces an oscillating $n = 1$ component into the dynamics, with frequency near Ω. In the frame of the substrate this state is a two-frequency state, as predicted by general theory, with the second frequency near ω_2 (the frequency of the traveling waves along the $n = 2$ branch).

The above considerations help us understand the origin of a number of surprising properties of the stability assignments along the $n = 1$ and $n = 2$ branches reported in Section 4, and give us confidence that these calculations were performed correctly.

References

[1] H.-C. Chang, Wave evolution on a falling film, Annu. Rev. Fluid Mech. 26 (1994) 103–136.

[2] A. Oron, S.H. Davis, S.G. Bankoff, Long-scale evolution of thin liquid films, Rev. Mod. Phys. 69 (1997) 931–980.

[3] M. Rabaud, Interface dynamics in the printer instability, Ann. Phys. Paris 19 (1994) 659–690.

[4] J. Burelbach, S. Bankoff, S. Davis, Nonlinear stability of evaporating/condensing liquid films, J. Fluid Mech. 195 (1988) 463–494.

[5] A. Oron, P. Rosenau, Formation of patterns induced by thermocapillarity and gravity, J. Phys. II France 2 (1992) 131–146.

[6] R.J. Deissler, A. Oron, Stable localized patterns in thin liquid films, Phys. Rev. Lett. 68 (1992) 2948–2951.

[7] A. Oron, Nonlinear dynamics of three-dimensional long-wave Marangoni instability in thin liquid films, Phys. Fluids 12 (2000) 1633–1645.

[8] A. Oron, P. Rosenau, On a nonlinear thermocapillary effect in thin liquid layers, J. Fluid Mech. 273 (1994) 361–374.

[9] S.J. VanHook, M.F. Schatz, J.B. Swift, W.D. McCormick, H.L. Swinney, Long-wavelength surface-tension-driven Bénard convection: experiment and theory, J. Fluid Mech. 345 (1997) 45–78.

[10] W. Boos, A. Thess, Cascade of structures in long-wavelength Marangoni instability, Phys. Fluids 11 (1999) 1484–1494.

[11] B. Ramaswamy, S. Chippada, S.W. Joo, A full-scale numerical study of interfacial instabilities in thin-film flows, J. Fluid Mech. 325 (1996) 163–194.
[12] D.J. Benney, Long waves on liquid films, J. Math. Phys. 45 (1966) 150–155.
[13] B. Gjevik, Occurrence of finite-amplitude surface waves on falling liquid films, Phys. Fluids 13 (1970) 1918–1925.
[14] S. Lin, Finite amplitude side-band instability of a viscous film, J. Fluid Mech. 63 (1974) 417–429.
[15] S.W. Joo, S.H. Davis, S.G. Bankoff, Long-wave instabilities of heated falling films: two-dimensional theory of uniform layers, J. Fluid Mech. 230 (1991) 117–146.
[16] S.W. Joo, S.H. Davis, Instabilities of three-dimensional viscous falling films, J. Fluid Mech. 242 (1992) 529–547.
[17] S.W. Joo, S.H. Davis, S.G. Bankoff, A mechanism for rivulet formation in heated falling films, J. Fluid Mech. 321 (1996) 279–298.
[18] S.H. Davis, Thermocapillary instabilities, Ann. Rev. Fluid Mech. 19 (1987) 403–435.
[19] A.A. Golovin, A.A. Nepomnyashchy, L.M. Pismen, Interaction between short-scale Marangoni convection and long-scale deformational instability, Phys. Fluids 6 (1994) 34–48.
[20] I.G. Kevrekidis, B. Nicolaenko, J.C. Scovel, Back in the saddle again—a computer-assisted study of the Kuramoto–Sivashinsky equation, SIAM J. Appl. Math. 50 (1990) 760–790.
[21] E.J. Doedel, A.R. Champneys, T. Fairgrieve, Y. Kuznetsov, B. Sandstede, X. Wang, AUTO97: continuation and bifurcation software for ordinary differential equations, Concordia University, Montreal, 1997.
[22] E. Doedel, H.B. Keller, J.P. Kernevez, Numerical analysis and control of bifurcation problems. I. Bifurcation in finite dimensions, Int. J. Bifurc. Chaos 1 (1991) 493–520.
[23] E. Doedel, H.B. Keller, J.P. Kernevez, Numerical analysis and control of bifurcation problems. II. Bifurcation in infinite dimensions, Int. J. Bifurc. Chaos 1 (1991) 745–772.
[24] C. Ruyer-Quil, P. Manneville, Improved modeling of flows down inclined planes, Eur. Phys. J. B 15 (2000) 357–369.
[25] U. Thiele, M.G. Velarde, K. Neuffer, Dewetting: Film rupture by nucleation in the spinodal regime, Phys. Rev. Lett. 87 (2001) 016104, 1–4.
[26] U. Thiele, K. Neuffer, Y. Pomeau, M.G. Velarde, On the importance of nucleation solutions for the rupture of thin liquid films, Colloid Surf. A 206 (2002) 135–155.
[27] U. Thiele, M.G. Velarde, K. Neuffer, M. Bestehorn, Y. Pomeau, Sliding drops in the diffuse interface model coupled to hydrodynamics, Phys. Rev. E 64 (2001) 061601, 1–12.
[28] U. Thiele, K. Neuffer, M. Bestehorn, Y. Pomeau, M.G. Velarde, Sliding drops on an inclined plane, Colloid Surf. A 206 (2002) 87–104.
[29] U. Thiele, E. Knobloch, Front and back instability of a liquid film on a slightly inclined plate, Phys. Fluids 15 (2003) 892–907.
[30] J.M. Skotheim, U. Thiele, B. Scheid, On the instability of a falling film due to localized heating, J. Fluid Mech. 475 (2003) 1–19.
[31] R.E. Ecke, F. Zhong, E. Knobloch, Hopf bifurcation with broken reflection symmetry in rotating Rayleigh–Bénard convection, Europhys. Lett. 19 (1992) 177–182.
[32] J.W. Cahn, J.W. Hilliard, Free energy of a nonuniform system. 1. Interfacial free energy, J. Chem. Phys. 28 (1958) 258–267.
[33] A. Novick-Cohen, L.A. Segel, Nonlinear aspects of the Cahn–Hilliard equation, Physica D 10 (1984) 277–298.
[34] A. Novick-Cohen, The nonlinear Cahn–Hilliard equation: transition from spinodal decomposition to nucleation behavior, J. Statist. Phys. 38 (1985) 707–723.
[35] V.S. Mitlin, Dewetting of solid surface: analogy with spinodal decomposition, J. Colloid Interf. Sci. 156 (1993) 491–497.
[36] A. Sharma, R. Khanna, Pattern formation in unstable thin liquid films, Phys. Rev. Lett. 81 (1998) 3463–3466.
[37] A. Oron, Three-dimensional nonlinear dynamics of thin liquid films, Phys. Rev. Lett. 85 (2000) 2108–2111.
[38] A.L. Bertozzi, G. Grün, T.P. Witelski, Dewetting films: bifurcations and concentrations, Nonlinearity 14 (2001) 1569–1592.
[39] U. Thiele, M.G. Velarde, K. Neuffer, Y. Pomeau, Film rupture in the diffuse interface model coupled to hydrodynamics, Phys. Rev. E 64 (2001) 031602, 1–14.
[40] A.A. Golovin, A.A. Nepomnyashchy, S.H. Davis, M.A. Zaks, Convective Cahn–Hilliard models: from coarsening to roughening, Phys. Rev. Lett. 86 (2001) 1550–1553.
[41] M. Eres, L. Schwartz, R. Roy, Fingering phenomena for driven coating films, Phys. Fluids 12 (2000) 1278–1295.
[42] M. Bestehorn, K. Neuffer, Surface patterns of laterally extended thin liquid films in three dimensions, Phys. Rev. Lett. 87 (2001) 046101, 1–4.
[43] S.G. Yiantsios, B.G. Higgins, Rayleigh–Taylor instability in thin viscous films, Phys. Fluids A 1 (1989) 1484–1501.
[44] H.-C. Chang, Onset of nonlinear waves on falling film, Phys. Fluids A 1 (1989) 1314–1327.
[45] L.T. Nguyen, V. Balakotaiah, Modeling and experimental studies of wave evolution on free falling viscous films, Phys. Fluids 12 (2000) 2236–2256.
[46] M. Golubitsky, D.G. Schaeffer, Singularities and Groups in Bifurcation Theory, vol. 1, Springer, New York, 1985.
[47] L.S. Tuckerman, D. Barkley, Bifurcation-analysis of the Eckhaus instability, Physica D 46 (1990) 57–86.
[48] I. Mercader, J. Prat, E. Knobloch, The 1:2 mode interaction in Rayleigh–Bénard convection with weakly broken midplane symmetry, Int. J. Bifurc. Chaos 11 (2001) 27–41.
[49] M.C. Depassier, E.A. Spiegel, The large-scale structure of compressible convection, Astron. J. 86 (1981) 496–512.
[50] P.C. Matthews, N.E. Hurlburt, M.R.E. Proctor, D.P. Brownjohn, Compressible magnetoconvection in oblique fields: linearized theory and simple nonlinear models, J. Fluid Mech. 240 (1992) 559–569.
[51] P. Ashwin, K. Böhmer, Z. Mei, Forced symmetry breaking of homoclinic cycles in a PDE with O(2) symmetry, J. Comput. Appl. Math. 70 (1996) 297–310.
[52] A. Schmiegel, B. Eckhardt, Fractal stability border in plane Couette flow, Phys. Rev. Lett. 79 (1997) 5250–5253.
[53] A. Schmiegel, B. Eckhardt, Persistent turbulence in annealed plane Couette flow, Europhys. Lett. 51 (2000) 395–400.
[54] L. Brusch, H. Kühne, U. Thiele, M. Bär, Dewetting of thin films on heterogeneous substrates: pinning vs. coarsening, Phys. Rev. E 66 (2002) 011602, 1–5.

[55] U. Thiele, L. Brusch, M. Bestehorn, M. Bär, Modelling thin-film dewetting on structured substrates and templates: bifurcation analysis and numerical simulations, Eur. Phys. J. E 11 (2003) 255–271.
[56] B. Scheid, A. Oron, P. Colinet, U. Thiele, J.C. Legros, Nonlinear evolution of nonuniformly heated falling liquid films, Phys. Fluids 14 (2002) 4130–4151.
[57] A.L. Bertozzi, M.C. Pugh, Finite-time blow-up of solutions of some long-wave unstable thin film equations, Indiana Univ. Math. J. 49 (2000) 1323–1366.
[58] O.A. Kabov, Heat transfer from a small heater to a falling liquid film, Heat Transfer Res. 27 (1996) 221–226.
[59] B. Scheid, O.E. Kabov, C. Minetti, P. Colinet, J.C. Legros, Measurement of free surface deformation by reflectance-Schlieren method, in: Proceedings of the Third European Conference on Heat Mass Transfer, Heidelberg, 2000.
[60] A. Oron, S.G. Bankoff, Dynamics of a condensing liquid film under conjoining/disjoining pressures, Phys. Fluids 13 (2001) 1107–1117.
[61] A. Oron, S.G. Bankoff, Dewetting of a heated surface by an evaporating liquid film under conjoining/disjoining pressures, J. Colloid Interf. Sci. 218 (1999) 152–166.
[62] A. Sharma, A.T. Jameel, Nonlinear stability, rupture and morphological phase separation of thin fluid films on apolar and polar substrates, J. Colloid Interf. Sci. 161 (1993) 190–208.
[63] D. Armbruster, J. Guckenheimer, P. Holmes, Kuramoto–Sivashinsky dynamics on the center-unstable manifold, SIAM J. Appl. Math. 49 (1989) 676–691.